HTGR SAFETY EVALUATION DIVISION

QUARTERLY REPORT
October 1 - December 31, 1975

DEPARTMENT OF APPLIED SCIENCE

BROOKHAVEN NATIONAL LABORATORY
ASSOCIATED UNIVERSITIES, INC.

UNDER CONTRACT NO. E(30-1)-16 WITH THE
UNITED STATES ENERGY RESEARCH AND DEVELOPMENT ADMINISTRATION

DISCLAIMER

BNL 50494
(Advanced Reactor Safety Research,
Gas-Cooled Reactors - NRC-8)

HTGR SAFETY EVALUATION DIVISION

QUARTERLY REPORT
October 1 - December 31, 1975

DONALD G. SCHWEITZER, Head
HTGR Safety Evaluation Division

The High Temperature Gas Cooled Reactor (HTGR) Safety Evaluation Division provides research and analytical support to the Nuclear Regulatory Commission (NRC), Office of Nuclear Regulatory Research (RSR), on all aspects of HTGR's regarding public safety. In addition to BNL personnel, the HTGR Safety Evaluation Division uses a wide national and international base of consulting expertise for RSR by close collaboration with consultants and subcontractors at universities and scientific establishments.

This work was performed under the auspices of the Nuclear Regulatory Commission Contract No. E(30-1)-16.

BROOKHAVEN NATIONAL LABORATORY
UPTON, NEW YORK 11973

EB

NOTICE

Printed in the United States of America
Available from
National Technical Information Service
U.S. Department of Commerce
5285 Port Royal Road
Springfield, VA 22161
Price: Domestic $7.00; Foreign $9.50;
Microfiche $2.25

March 1976 385 copies

TABLE OF CONTENTS

TABLE OF CONTENTS - Cont'd.

Summary

The construction of the apparatus for measuring cesium desorption from H451 graphite using a Knudsen effusion radiotracer technique was completed and preliminary experiments using elemental cesium were carried out to assess the reliability of the apparatus. The cesium vapor pressures computed from the experimental results obtained were in excellent agreement with published vapor pressures. The next series of experiments will involve the cesium-graphite system. A limited thermochemical data evaluation has been carried out to determine the possibility of formation of volatile fission metal carbonyls. Experiments to study iodine sorption and diffusion in PCRV concrete are planned in the near future. Calculations are continuing to study volatile fission product oxide-hydroxide formation. The work completed can be divided into two areas:

1. Ratio of hydroxide to element vapor pressure as a function of temperature.
2. Relative tendency to form gaseous hydroxide in a thermodynamically closed system for a certain water vapor partial pressure.

Within the temperature range studied (300° to $2000^{\circ}K$) the fission products which are most hydrolyzable into a gaseous hydroxide (without carbon) are cesium, strontium and cerium.

The Helium Impurities Loop (HIL) was operated without specimens in place at various conditions including the anticipated design

conditions. Measurements of impurities in the loop were made with a gas chromatograph and correlated with a ZrO_2-Y_2O_3 electrolyte oxygen activity meter. Several modifications were required in the H_2O injection and impurity monitoring systems in order to improve the control and measurement of impurities. Following the modifications, graphite tensile test specimens (H451, PGX and ATJ) were installed and exposure has been started. Operation of the HIL offered an opportunity to demonstrate the sensitivity of the electrochemical oxygen meter. The meter was found to be very responsive to impurity changes in the loop. A calibration curve (compared to gas chromatograph measurements) for the meter was generated during oxygen transients in the loop. The curve is near theoretical at oxygen concentrations down to about 200 ppmv. At high concentrations of H_2 in the system, large deviations from ideality were observed. However, under those conditions the behavior of the meter should be predicted by the H_2/H_2O and CO/CO_2 ratios. The activity meter potential was correlated with the loop's partial pressure of oxygen (during an oxygen transient) to calculate rate of reaction of oxygen with H451 graphite in the loop. A value of 1.5×10^{-4} $g/cm^2\text{-}h^{-1}\text{-}atm^{-1}$ was calculated as compared to air oxidation of H451 graphite in static tests which gave a value of 1.3×10^{-4} $g/cm^2\text{-}h^{-1}\text{-}atm^{-1}$.

An inert atmosphere glove box has been put into operation in which fuel handling and other inert atmosphere operations can be carried out. A shipment of bare weak acid resin kernels was received from ORNL. Experiments are being planned in which reactivity measure-

ments of various batches of fuels will be made.

An experimental program is under way in which Mössbauer spectroscopy is being employed to characterize the form of Fe in as received and oxidized PGX graphite. Preliminary results indicate that elemental Fe is the form present in as received graphites but that Fe_3O_4 is the form present in graphite oxidized in a 2% H_2O-He mixture for two weeks at 650°C. Further, pre-oxidized graphite exposed to a H_2-He mixture was found to contain elemental Fe. Preliminary measurements of graphite oxidation rates using a Cahn recording microbalance have given a value of 1.3×10^{-4} $g/cm^2\text{-}h^{-1}\text{-}atm^{-1}$ for H451 graphite exposed in air at 550°C for 20 hours. A log of ATJ graphite has been sampled at 200 random locations and the samples are presently being analyzed by the standard emission spectrographic method.

A seven mass horizontal array model of the entire core using an unequal mass distribution was developed and evaluated. The model is symmetric, consistent with the true core support block boundaries and includes an elastic link with adjustable gap connections between the reflector blocks. Core response characteristics were found to vary as a function of the nature of the link between the reflector blocks. Development of a three dimensional finite element stress code suitable for PCRV analyses continues. The code uses isoparametric elements and incorporates failure criteria that accounts for biaxial or triaxial tensile cracking and compressive crushing of the concrete together with elastic-plastic behavior of the steel. Current work

extending the method to include dynamic capabilities using a "staggered" time integration scale for computation of the velocity is also under way.

The assessment of the adequacy of HTGR materials data properties is continuing. Detailed literature surveys are in progress and relevant information on Incoloy 800H, Hastelloy-X and ATJ graphite physical and mechanical properties is being tabulated. A status report will be issued shortly. A single 1400^{o}F fatigue test on a new heat of Incoloy 800H containing 0.07 wt percent carbon is in progress, and it appears to have a fatigue life at least as high as the old heat which contained 0.03 wt percent carbon. A comparison between the properties was performed for normal concretes and those prepared by the preplaced aggregate concrete (PAC) technique. Various differences were emphasized and areas where additional study are required are cited. Crack propagation and oxidation studies on several candidate graphites for HTGR applications are also proceeding. Scanning electron microscopy studies indicate that in PGX graphite the crack paths tend to follow the pores which outline dense regions. Oxidation studies in air at temperatures up to 550^{o}C show that ATJ graphite has approximately double the weight loss of PGX graphite. Attendant changes in microstructures arising from the oxidation are being investigated.

An experimental program involving the application of a mass spectrometer to measure impurities in the primary coolant of Fort St. Vrain is proposed. The mass spectrometer being considered would measure

Xe, Kr, Ar, Cs and I at concentrations of 1 ppbv and H_2, tritium, CH_4, O_2, N_2, H_2O, CO and CO_2 at 1 ppmv. An alternate instrument proposed as an impurity monitor at Fort St. Vrain is the electrochemical oxygen meter.

The OXIDE-3 code is used to study the effects of accidental inleakage of air and/or steam into the primary coolant system. The central part of the code involves a finite difference calculation on a mesh which is solved for some 200 different graphite core elements. The accuracy of the calculation is dependent upon the mesh spacing and evidence is presented which shows that the OXIDE-3 mesh appears suspect regarding the air-ingress calculation. An initial alternative mesh is shown based upon the evidence. In the area of Phenomena Modeling and Systems Analysis, computer code improvement, development and analysis was achieved. The GOPTWO program was extended in capability so that any finite mass transfer coefficient can now be accommodated. A diffusion theory code was developed based on the finite element technique that is effective in heat transfer, neutron diffusion, and fission product migration problems. A rudimentary program that simulates reactor plant systems has also been developed to test modules that will be incorporated into the TFR systems code. Sample problems have been run with both of these new programs.

Reactor physics calculations have been made on the HTR Control Rod Fuel Assembly. Fuel zoning and mesh point spacing on specific materials has been studied. A two dimensional DS_N calculational system

has been set up to generate homogenized two group diffusion theory parameters for HTR Control Rod Fuel Assemblies. Results of a typical Control Rod Assembly at operating temperature are tabulated.

1. Task Area I - Fission Product Release and Transport

1.1 Diffusion of Cs in Graphite (R. Behrens, S. Aronson - Brooklyn College)

1.1.1 Experimental

Prior to introduction of a new sample of elemental cesium into the molybdenum crucible, the cesium from the first experiment was removed by dissolving it in butanol. A new sample of tagged cesium metal weighing 87.9 milligrams was then placed in the crucible and the lid and bottom cemented together using a low vapor pressure resin conventionally used as a leak sealant in high vacuum systems. It was hoped that this would prevent cesium leakage from the space between the crucible lid and bottom. A plug of paraffin wax was placed in the orifice and the crucible transferred from the dry box to the vaporization apparatus.

The procedure for measuring the rate of mass loss of the cesium was the same as that described in our previous progress report. Rate measurements were made over the temperature range 379-428^{o}K. The data are presented in Table 1-1 along with vapor pressures computed from the Hertz-Knudsen-Langmuir equation. Our experimental vapor pressures are shown in Figure 1-1 where they are compared with literature data. A least-squares fit of the data gives values for the enthalpy and entropy of vaporization for the reaction Cs(l) = Cs(g) of $\Delta H^{o}(408K)$ = 17.90 kcal mole^{-1} and $\Delta S^{o}(408K)$ = 18.88 cal K^{-1} mole^{-1}. Using published thermodynamic functions for Cs(g)[1-1]

Table 1-1

Data for the Vaporization of Liquid Cesium:

$Cs(l) = Cs(g)$, $\underline{a} = 4.989 \times 10^{-3}$ cm^2, $\underline{W}_a = 0.7189$

Point No.	T(^{o}K)	Rate of Mass Loss (mg/min^{-1})	$-\log_{10}P$(atm)	$\Delta H^{o}(298^{o}K)$ (kcal mole^{-1}
2	411.47	0.01427	5.580	19.17
3	416.93	0.02912	5.267	18.82
4	422.86	0.05770	4.967	18.50
5	427.92	0.6150	4.937	18.65
6	407.96	0.02035	5.427	18.73
7	402.65	0.01067	5.711	19.02
8	397.69	0.00829	5.823	18.99
9	379.19	0.00521	6.035	18.52

$\Delta H^{o}(408^{o}K) = 17.90$ kcal mole^{-1}

$\Delta S^{o}(408^{o}K) = 18.88$ cal K^{-1} mole^{-1}

$\Delta H^{o}(298^{o}K) = 18.69$ kcal mole^{-1} Second-law

$\Delta H^{o}(298^{o}K) = 18.80$ kcal mole^{-1} Third-law

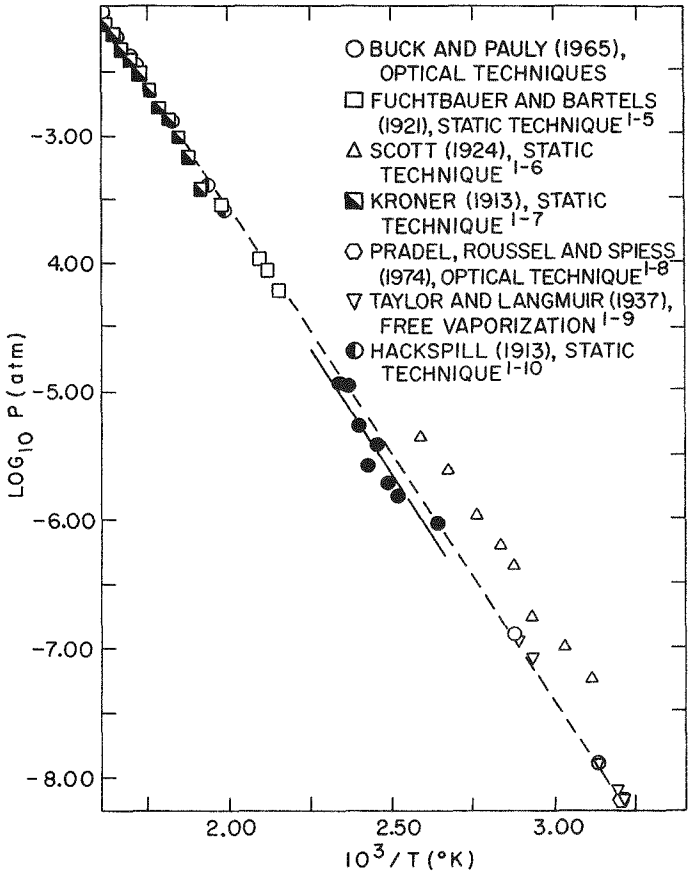

Figure 1-1. Plot of present and literature vapor pressures for the reaction Cs(1) = Cs(g). Dark circles and solid line represent the present data. Dashed line represents vapor pressures computed from $H^{o}(298K)$ = 18.46 kcal $mole^{-1}$ and free energy functions for Cs(1) and Cs(g). Other points represent literature data.

and Cs(l)[1-2] a second-law value of ΔH^{o}(298, second-law) = 18.69 kcal mole^{-1} and a third-law value of ΔH^{o}(298, third-law) = 18.80 kcal mole^{-1} are obtained from the present vapor pressure data. The second- and third-law values of ΔH^{o}(298) are in excellent agreement with one another and with the third-law value of ΔH^{o}(298) = 18.46 kcal mole^{-1} arrived at in our previous review of the literature cesium vapor pressure data[1-3].

The quality of the results for elemental cesium indicate that the apparatus should be capable of yielding accurate data for the cesium-graphite system. However, the study of elemental cesium yielded vapor pressures only as low as 10^{-6} atmospheres. Measurements to 10^{-9} atmospheres will be required in the cesium-graphite studies. We are presently preparing to perform one final study of elemental cesium in the pressure range of 10^{-6} to 10^{-9} atmospheres. A new molybdenum effusion cell has been constructed with a larger orifice area and another sample of cesium has been irradiated to three times the activity of the sample used in the initial experiments.

1.1.2 Thermochemical Data Evaluation

It has been suggested[1-11] that formation of volatile carbonyl compounds of the fission metals molybdenum, ruthenium, and technetium may limit deposition of these fission products in cooler regions of the reactor coolant circuit. Because of a potential need for the high temperature thermodynamic properties of these compounds

we have reviewed the literature for pertinent thermochemical information as well as for data needed to compute thermodynamic functions for the gaseous molecules.

Table 1-2 summarizes literature values for the enthalpies of formation, $\Delta H_f^o(298K)$ of some condensed and gaseous metal carbonyls of the group VIB, VIIB and VIIIB transition metals. Values for condensed $Tc_2(CO)_{10}$ and for gaseous $Tc_2(CO)_{10}$, $Ru(CO)_5$, and $Os(CO)_5$ have been estimated.

Virtually nothing is known concerning absolute entropies of the condensed phases of the carbonyls. The heat capacity of iron pentacarbonyl has been investigated between 50^oK and 280^oK but no other thermodynamic functions have been computed for it. Thermodynamic functions for $Cr(CO)_6(g)$, $Mo(CO)_6(g)$ and $W(CO)_6(g)$, $Fe(CO)_5(g)$ and $Ni(CO)_4(g)$ have been reported in the literature. The vapor pressure of chromium, molybdenum, and tungsten hexacarbonyls, ironpentacarbonyl, and nickel tetracarbonyl have been reported in the literature and thus will enable calculation of the condensed phase thermodynamic functions as the gas phase properties are known.

Thermal functions for all the gaseous carbonyls listed in Table 1-2 have been computed with the exception of $Ni(CO)_4(g)$ but have only reported the results for $Mo(CO)_6$, $Tc_2(CO)_6$, and $Ru(CO)_5$ here (Table 1-3).

Based on the entropies in Table 1-3 and entropies for the elements from reference 1-1 the standard Gibbs free energy of

Table 1-2

Standard Enthalpies of Formation, $\Delta H_f^o(298^oK)$ for

Transition Metal Carbonyls

	$Cr(CO)_6$	$Mn_2(CO)_{10}$	$Fe(CO)_5$	$Ni(CO)_4$
Condensed Phase	-257	-401	-185	-151
Vapor	-240	-382	-175	-144

	$Mo(CO)_6$	$Tc_2(CO)_{10}$	$Ru(CO)_5$
Condensed Phase	-235	(-398)	----
Vapor	-218	(-377)	(-175.4)

	$W(CO)_6$	$Re_2(CO)_{10}$	$Os(CO)_5$
Condensed Phase	-228	-395	----
Vapor	-208	-373	(-175)

Table 1-3

Standard Thermodynamic Functions for $Mo(CO)_6(g)$, $Ru(CO)_5(g)$ and $Tc_2(CO)_{10}(g)$

	T(°K)	C_p^o (cal K^{-1} $mole^{-1}$)	$H^o(T) - H^o(298)$ [a] cal $mole^{-1}$	$S^o(T)$ (cal K^{-1} $mole^{-1}$)	$-[G^o(T) - H^o(298)]/T$ (cal K^{-1} $mole^{-1}$)
$Mo(CO)_6(g)$	298.15	50.34	0	120.11	120.11
	400	55.05	5388	135.62	122.15
	500	58.09	11053	148.25	126.14
	600	60.46	16984	159.06	130.75
	700	62.40	23130	168.53	135.48
	800	64.01	29453	176.97	140.15
	900	65.35	35923	184.59	144.67
	1000	66.47	42516	191.53	149.02
	1100	67.39	49210	197.91	153.17
	1200	68.16	55989	203.81	157.15

(a) $H^o(298) - H^o(0) = 9941$ cal $mole^{-1}$

$Ru(CO)_5(g)$	298.15	42.29	0	110.45	110.45
	400	46.25	4527	123.48	112.16
	500	48.77	9285	134.09	115.52
	600	50.72	14263	143.16	119.39
	700	52.32	19417	151.10	123.36
	800	53.66	24718	158.18	127.28
	900	54.77	30141	164.56	131.07
	1000	55.70	35666	170.38	134.72
	1100	56.47	41275	175.73	138.21
	1200	57.11	46955	180.67	141.54

(a) $H^o(298) - H^o(0) = 8365$ cal $mole^{-1}$

Table 1-3 - Cont'd.

	T(°K)	C_p^o (cal K^{-1} $mole^{-1}$)	$H^o(T) - H^o(298)$ [a] cal $mole^{-1}$	$S^o(T)$ (cal K^{-1} $mole^{-1}$)	$-[G^o(T) - H^o(298)]/T$ (cal K^{-1} $mole^{-1}$)
$Tc_2(CO)_{10}(g)$	298.15	82.91	0	160.74	160.74
	400	92.56	8977	164.13	164.13
	500	98.78	18562	207.94	170.81
	600	103.44	28682	226.38	178.57
	700	107.16	39219	242.61	186.58
	800	110.18	50091	257.12	194.51
	900	112.65	61236	270.25	202.21
	1000	114.67	72605	282.22	209.62
	1100	116.34	84158	293.23	216.73
	1200	117.72	95864	303.42	223.53

(a) $H^o(298) - H^o(0) = 15476$ cal $mole^{-1}$

formation, $\Delta G_f^o(T)$ has been computed for the gaseous molecules at 500^oK and 1000^oK:

$Mo(CO)_6(g)$	$\Delta G_f^o(500K)$	=	-197 kcal $mole^{-1}$
	$\Delta G_f^o(1000K)$	=	-181 kcal $mole^{-1}$
$Ru(CO)_5(g)$	$\Delta G_f^o(500K)$	=	-163 kcal $mole^{-1}$
	$\Delta G_f^o(1000K)$	=	-153 kcal $mole^{-1}$
$Tc_2(CO)_{10}(g)$	$\Delta G_f^o(500K)$	=	-325 kcal $mole^{-1}$
	$\Delta G_f^o(1000K)$	=	-270 kcal $mole^{-1}$

The stabilities of these molecules with respect to the elements may be compared with the stabilities of gaseous oxides, and hydroxides of Mo, Ru and Tc summarized in Table 1-4.

1.2 The Permeability and Retentivity of Stressed Concrete Relative to Fission Product Iodine (L. R. Zumwalt, J. Mirza - North Carolina State University)

The initial effort is to be directed at the study of the sorption behavior of iodine in concrete. The data obtained will give the maximum iodine loading of concrete samples for selected iodine vapor pressure and temperature conditions. Rates of sorption will also be determined.

Concurrent with the establishment of sorption behavior, steps will be taken so that permeation experiments can be carried out. Initial work to be done in this regard is described below.

1.2.1 Iodine Sorption in Concrete

The concrete samples to be used will be small pieces

Table 1-4

Summary of Standard Gibbs Free Energy of Formation for Gaseous Molybdenum, Ruthenium and Technetium Oxides and Hydroxides

Gaseous Molecule	$\Delta G_f^o(T)$ (kcal mole^{-1}) 500°K	1000°K
Mo	+140	+123
MoO	+ 76	+ 65
MoOH	+ 64	+ 58
MoO_2	- 4	- 8
$Mo(OH)_2$	- 35	- 25
MoO_3	- 74	- 67
$MoO_2(OH)_2$	-178	-153
$(MoO_3)_2$	-238	-202
$(MoO_3)_3$	-402	-336
Ru	+136	+117
RuO	+ 90	+ 76
RuOH	+ 71	+ 64
RuO_2	+ 40	+ 44
$Ru(OH)_2$	+ 5	+ 14
RuO_3	- 9	- 1
RuO_4	- 27	- 8
Tc	+137	+120
TcO	+ 76	+ 65
TcOH	+ 72	+ 66
TcO_2	+ 18	+ 12
$Tc(OH)_2$	- 8	+ 3
Tc_2O_7	-192	-137

or chunks broken down from larger specimens. Before sorption experiments, the BET surface areas of representative samples will be determined. The primary method to be employed will be sorption of iodine on concrete in an evacuated system (Figure 1-2) following an approach used by Anderson, Wessman and Zumwalt[1-12]. Iodine will behave as a Knudsen gas at low vapor pressures in this experiment. The source of this iodine will be a bed of iodine crystals maintained at constant temperature, which will thereby provide a selected and fixed equilibrium partial pressure.

A calibrated scintillation detector mounted directly under the concrete samples will monitor the deposition of iodine on the bed continuously. Knowing the counting efficiency of the detector and the specific activity of the iodine, one can then calculate the amount of iodine sorbed in concrete at any time. The experiment will be continued until the scintillation detector indicates no further deposition of iodine on the bed. At this point, the equilibrium pressure of the iodine sorbed in the concrete will be approximately equal to the iodine partial pressure of the source. The temperature of the concrete bed will be varied from room temperature (25-30^{o}C) to 150^{o}C. Vapor pressures of iodine to be employed by these experiments will be varied from approximately 10^{-3} atmospheres to 10^{-7} atmospheres. Attempts will be made to go to lower vapor pressures, but experimental limitation may preclude this possibility.

A second method will be employed, though perhaps somewhat less extensively, to study the sorption behavior. This will

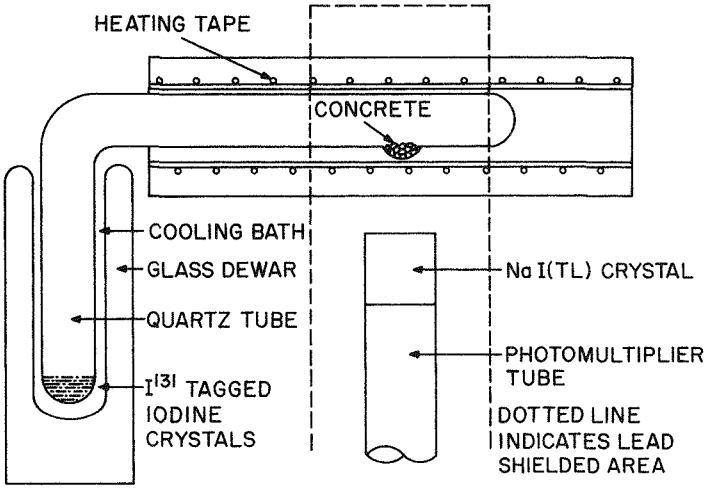

Figure 1-2. Static sorption apparatus.

utilize a dynamic method using helium gas to transport iodine over a small bed (Figure 1-3). By using rather slow flow rates (10 ml/min) of helium over a bed of iodine crystals, maintained at constant temperature, equilibrium partial pressures of iodine can be obtained readily. All other parts of the system will be similar to those of the primary system. The helium will be allowed to flow until the scintillation detector under the concrete sample bed indicates no further deposition.

1.2.2 Test Specimens and Structural Loading System

The initial phase of the project will be devoted to planning and designing the concrete test specimens, the test frame, and a load application and remote monitoring system.

Aggregates for the concrete mix will be selected such that there is chemical similarity with typical prototypes. Ingredients will be proportioned to produce compressive strength, slump, and density similar to prevailing concrete reactor vessel practice. It may be necessary, however, to scale down coarse aggregate size.

Depending upon the size of the test specimens, a load application system consisting of hydraulic jack, pump, and test frame will be designed, with sufficient factor of safety. Load monitoring will be done by use of a load cell and compatible readout equipment. The entire system will be thoroughly calibrated before experimental application.

The test frame will be designed to provide a safety factor of at least 2 against maximum expected jacking loads. The

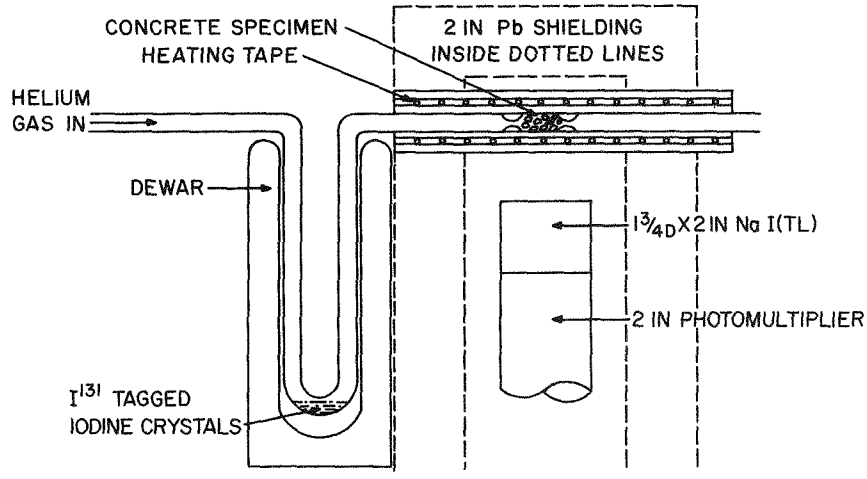

Figure 1-3. Dynamic sorption apparatus.

steel members will be sized to be compatible with the available shielded working space.

1.3 Fission Product Hydrolysis and Oxidation (D. Chandra)

Based on existing thermodynamic data[1-13,1-14], calculations are continuing to study volatile fission product oxide/hydroxide formation. The work done so far can be divided into two areas:

1. Ratio of hydroxide to element vapor pressures as a function of temperature and water vapor partial pressure, with and without carbon.

2. Relative tendency to form gaseous oxide/hydroxides in a thermodynamically closed system for a certain water vapor partial pressure, with and without carbon.

1.3.1 Hydroxide to Element Vapor Pressure Ratio

The work completed so far refers only to the case where carbon is absent. The following reactions were considered:

$$M_v + H_2O \overset{K_1}{\rightleftarrows} MOH_v + \tfrac{1}{2}H_2 \qquad (1)$$

and

$$M_v + 2H_2O \overset{K_2}{\rightleftarrows} M(OH)_{2_v} + H_2 \qquad (2)$$

and vapor pressure ratios can be expressed as:

$$\frac{P_{MOH}}{P_M} = K_1 \cdot \frac{P_{H_2O}}{P_{H_2}^{\frac{1}{2}}} \qquad (3)$$

and

$$\frac{P_{M(OH)_2}}{P_M} = K_2 \cdot \frac{P_{H_2O}^2}{P_{H_2}} \qquad (4)$$

and the equilibrium constants can be estimated from the familiar equation:

$$K = \exp\left(-\frac{\Delta G}{RT}\right) \tag{5}$$

where ΔG is the standard free energy change for the reaction under consideration.

Figure 1-4 shows the vapor pressure ratios for a water vapor partial pressure of 5×10^{-3} atmospheres (100 ppm H_2O in 50 atmospheres helium) as a function of temperature. For almost all the fission products, $M(OH)_2$ is the dominant species. For some fission products $M(OH)_2$ becomes less dominant than M(OH) over a certain temperature.

The basic usefulness of this series of calculations lies in pinpointing what dominant species of hydroxides is to be considered for subsequent more thorough analysis. It should be noted that the ordinate in Figure 1-4 refers only to a ratio, not absolute values. Therefore, this cannot provide information regarding what fraction of a particular element will hydrolyze into a volatile product.

1.3.2 Relative Tendency to Form Gaseous Hydroxide

This series of calculations was carried out to estimate the relative ability of different fission products to form volatile hydroxides. The estimates were made as follows:

$$M_{s,\ell} + H_2O \overset{K_3}{\rightleftarrows} MOH_v + \tfrac{1}{2}H_2 \tag{6}$$

$$\tfrac{1}{2}M_{s,\ell} + H_2O \overset{K_4}{\rightleftarrows} \tfrac{1}{2}M(OH)_{2_v} + \tfrac{1}{2}H_2 \tag{7}$$

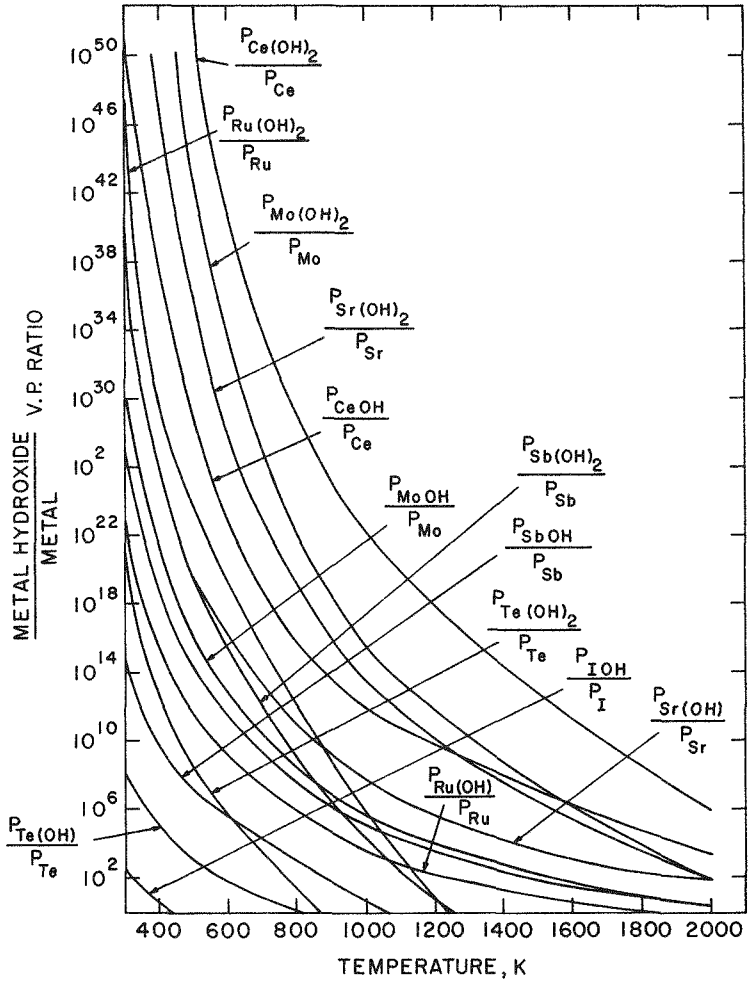
METAL HYDROXIDE / METAL V.P. RATIO
TEMPERATURE, K
$P_{Ce(OH)_2}/P_{Ce}$
$P_{Ru(OH)_2}/P_{Ru}$
$P_{Mo(OH)_2}/P_{Mo}$
$P_{Sr(OH)_2}/P_{Sr}$
P_{CeOH}/P_{Ce}
P_{MoOH}/P_{Mo}
$P_{Sb(OH)_2}/P_{Sb}$
P_{SbOH}/P_{Sb}
$P_{Te(OH)_2}/P_{Te}$
P_{IOH}/P_{I}
$P_{Sr(OH)}/P_{Sr}$
$P_{Ru(OH)}/P_{Ru}$
$P_{Te(OH)}/P_{Te}$
10^{50}
10^{46}
10^{42}
10^{38}
10^{34}
10^{30}
10^{2}
10^{22}
10^{18}
10^{14}
10^{10}
10^{6}
10^{2}
400 600 800 1000 1200 1400 1600 1800 2000

Figure 1-4.

A closed system was assumed for these reactions. Therefore, the water vapor amount was finite and the reaction products could not be removed from the system. The fraction of water converted when equilibrium was reached was computed as follows:

Let y = initial partial pressure of water vapor, x = amount of water converted when equilibrium was reached, then equation (6) can be rewritten as:

$$K_3 = \frac{x \cdot (\frac{x}{2})^{\frac{1}{2}}}{(y - x)} \qquad (8)$$

and

$$K_4 = \frac{(\frac{x}{2})^{\frac{1}{2}} \cdot (\frac{x}{2})^{\frac{1}{2}}}{(y - x)} \qquad (9)$$

These equations can then be solved for x at a certain temperature and a certain initial partial pressure of water y. The ratio $\frac{x}{y}$ will then be the fraction of water converted at equilibrium and thus indicate the relative hydrolyzability of the fission products in a closed system. It should be noted that it does not provide any information with respect to the kinetics of the reaction. These values are plotted in Figure 1-5.

Within the temperature range studied the fission products which were most hydrolyzable into a gaseous hydroxide are cesium, cerium, and strontium. The species of gaseous hydroxides formed are CsOH, $Ce(OH)_2$, and $Sr(OH)_2$.

These calculations are continuing to include:

1. Formation of more complex hydroxides and oxyhydroxides.
2. Influence of carbon.
3. Influence of changing partial pressures of water vapor.

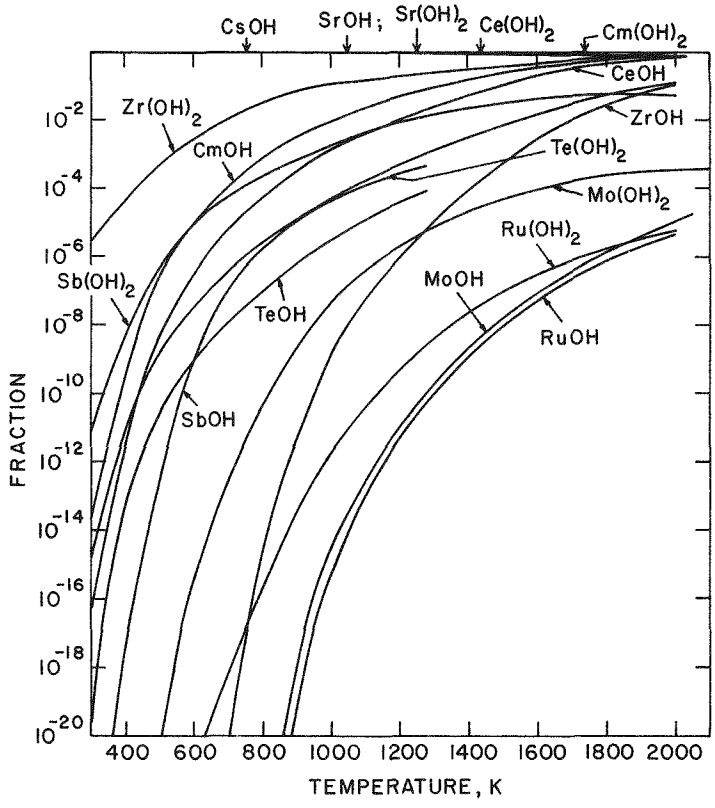
CsOH
SrOH; Sr(OH)2
Ce(OH)2
Cm(OH)2
CeOH
ZrOH
Te(OH)2
Mo(OH)2
Ru(OH)2
Zr(OH)2
CmOH
Sb(OH)2
TeOH
MoOH
RuOH
SbOH
FRACTION
10-2
10-4
10-6
10-8
10-10
10-12
10-14
10-16
10-18
10-20
400 600 800 1000 1200 1400 1600 1800 2000
TEMPERATURE, K

Figure 1-5.

References

1-1 R. Hultgren, P. D. Desai, D. T. Hawkins, M. Gleiser, K. K. Kelley and D. D. Wagman, Selected Values of the Thermodynamic Properties of the Elements. ASME, Metals Park, Ohio, 1973.

1-2 R. G. Behrens and S. Aronson, HTGR Safety Evaluation Division Quarterly Progress Report, January-March, 1975, BNL-50450.

1-3 R. G. Behrens and S. Aronson, HTGR Safety Evaluation Division Quarterly Progress Report, July-September, 1975, BNL-50479.

1-4 U. Buck and H. Pauly, Z. Phys. Chemie, N.F. 44, 345 (1965).

1-5 C. Fuchtbauer and H. Bartels, Z. Physik. 4, 337 (1921).

1-6 D. Scott, Phil. Mag. 47, 32 (1924).

1-7 A. Kroner, Ann. Physik. 40, A438 (1913).

1-8 P. Pradel, F. Roussel and G. Spiess, Rev. Sci. Instrum. 45, 45 (1974).

1-9 J. Taylor and I. Langmuir, Phys. Rev. 51, 423 (1937).

1-10 M. L. Hackspill, Ann. Chim. et Phys. 28, 6 (1913).

1-11 Planning Guide for HTGR Safety and Safety-Related Research and Development, Oak Ridge National Laboratory Report ORNL-4968, May 1974.

1-12 E. E. Anderson, G. L. Wessman and L. R. Zumwalt, "Iodine Adsorption in Activated Charcoal at Low Partial Pressures." Proc. Nucl. React. Chemistry, First Conference, Gatlinburg, Tenn., pp. 32-43, October 12-14, 1960, TID-7610.

References - Cont'd.

1-13 R. G. Bedford and D. D. Jackson, "Volatilities of Fission Product and Uranium Oxides," UCRL-12314.

1-14 D. D. Jackson, "Thermodynamics of Gaseous Hydroxides," UCRL-51137.

2. Task Area II - Primary Coolant Impurities

2.1 Helium Impurities Loop (A. Romano)

During this report period the Helium Impurities Loop (HIL) was operated at various conditions including the previously reported[2-1] design temperatures, flows and impurity levels. For these runs the graphite tensile specimens were not installed in the test section.

The initial runs consisted of engineering proof testing of the various components and systems in the HIL. Following these initial tests, the loop was shut down, and several modifications and repairs were made. The modifications included (1) installing a single column gas chromatograph having a thermal conductivity detector, (2) installing an oxygen activity meter having a ZrO_2-Y_2O_3 electrolyte, (3) installing a bypass around the molecular sieve tank, and (4) adding the impurity injection system. The modifications are given in the revised schematic drawing shown in Figure 2-1.

Another series of runs were then performed in which additions of impurities (water, air and oxygen) were made to the HIL. For these tests, the loop was operated at maximum temperatures of from 500 to 750°C for approximately 50 hours over a 5-day period. A brief summary of the operation is as follows:

Date	Max. Temp., °C	Impurity Injected	Flow Circuit
11/14	525	Air	Graphite
	525	H_2O	Graphite
11/17	700	None	Graphite
11/18	750	H_2O	Graphite
	750	O_2	Bypass

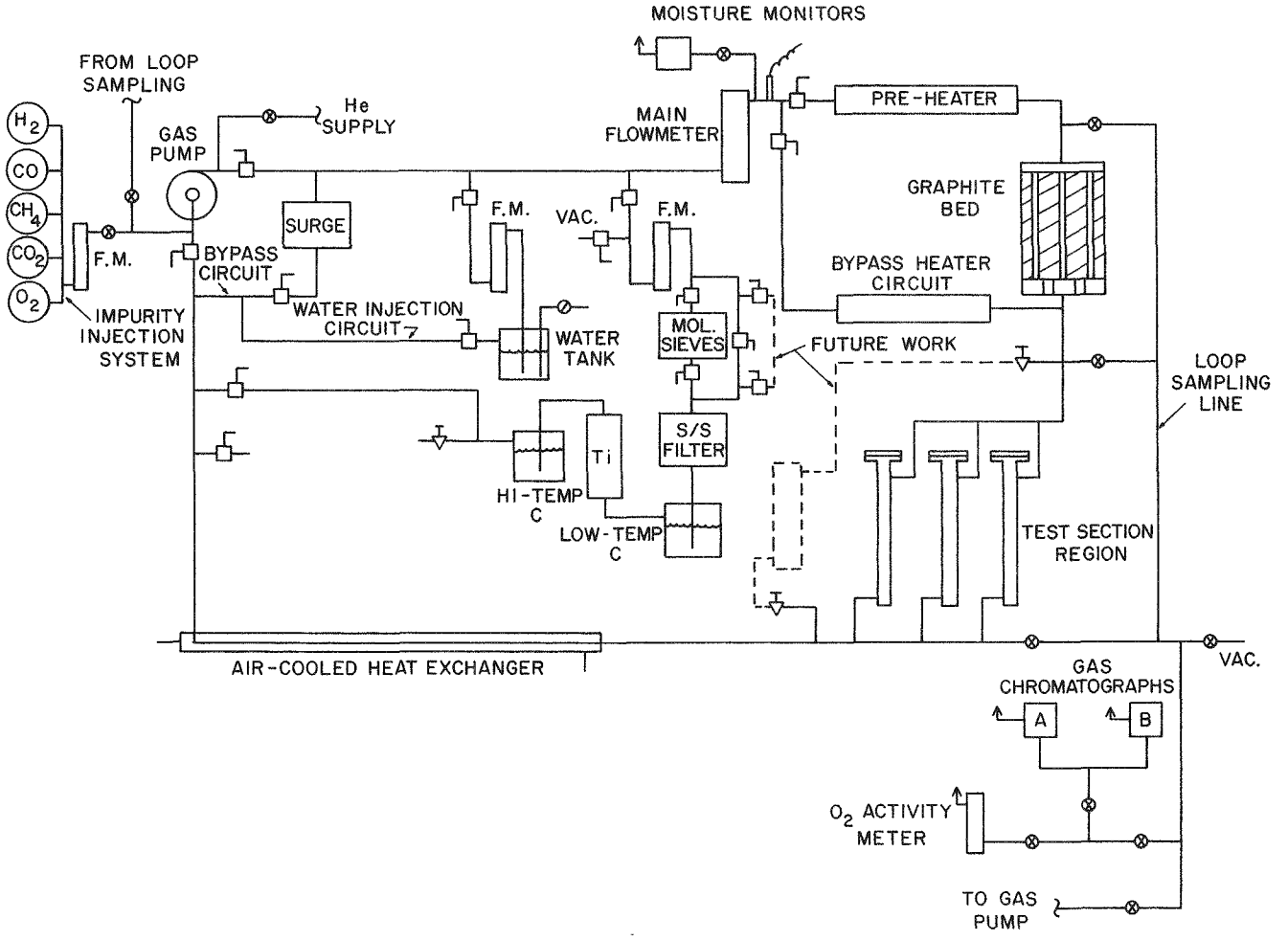

Figure 2-1. Helium impurities loop (schematic flow sheet).

11/19	550	O_2	Both
11/20	700	H_2O	Both

On 11/17 the loop pump was run overnight, whereas on all other days, circulation of He was stopped at the end of the day. The flow circuits referred to above are the graphite bed and bypass heater circuits respectively (see Figure 2-1).

Additions of impurities were monitored with the O_2 activity meter and gas chromatograph. The meter appears to be very sensitive to impurity additions made to the loop and is also responsive to removal of impurities by loop walls, the graphite bed and the purification system. Results from the activity meter measurements will be discussed in detail in the following section, 2.2 Impurity Monitoring.

The results from these runs must be considered qualitative. The difficulty was that the single column (6-foot-molecular sieve Linde 4A) gas chromatograph could only resolve H_2, O_2, N_2, CH_4 and CO, but not CO_2 and H_2O. With the use of calibrated gas mixtures, it was additionally found that the respective sensitivities varied considerably. For example, the minimum detectable limit of the instrument was ~10 ppmv O_2 or N_2, ~20 ppmv CH_4, ~40 ppmv CO but only ~500 ppmv H_2. However, several qualitative conclusions may be drawn from the experiments carried out:

(1) Impurity injections were performed by bubbling He through water and by injecting pure constituents from gas cylinders. It was found that both methods were adequate, but the H_2O injection rate

was very high relative to the reaction rate. This resulted in very high equilibrium concentrations of H_2O in the loop and concomitant CO, H_2 and CH_4 concentration levels. Typical maximum concentrations estimated and/or measured at selected times are given in Table 2-1.

(2) The removal of H_2O by molecular sieves and H_2 by Ti-Zr turnings appears to be adequate. Purification of the other impurities (CO, CO_2, CH_4, etc.) by cold trapping on activated charcoal was not attempted at this time.

(3) The optimum Ti-Zr temperature for removal of H_2 and O_2 simultaneously is about 150°C. At higher temperatures, O_2 is gettered more rapidly but H_2 is released from the Ti-Zr.

(4) On 11/20, the loop was operated in the manner anticipated when the specimens will be installed in place. The He was passed through both the graphite bed circuit (80% of main flow) and the bypass heater circuit (20% of the flow). Water was continuously injected by bubbling He through the H_2O tank and the H_2 produced was removed simultaneously. Again the flow of H_2O into the loop was higher than desired resulting in high equilibrium concentrations of H_2 and H_2O. These results are also summarized in Table 2-1.

(5) The observations indicated that further refinements were required on the loop monitoring and H_2O injecting systems. Modifications have since been made and are discussed below.

Modifications have been made to the H_2O injection system so that lower rates can be achieved. The most significant of the changes

Table 2-1

Concentrations of Impurities in HIL During Preliminary Test Runs

Date	Case No.	Maximum Concentrations[1], ppmv	Description of Event
11/14	I	3,800 H_2, (34,000 O_2)*, 500 CO, 80 CH_4	Following single burst air ingress.
11/14	II	n.d. H_2, 200 O_2, n.d. CO, 80 CH_4	Following 95-minute purification.
11/14	III	2,500 H_2, 200 O_2, n.d. CO and CH_4	Following single burst H_2O ingress.
11/18	IV	n.d. H_2, 500 O_2, n.d. CO and CH_4	Starting condition after purification.
11/18	V	11,000 H_2, 400 O_2, trace CH_4, (25,000 H_2O)*	Following single burst H_2O ingress.
11/19	VI	500 H_2, 75 O_2, n.d. CO and CH_4	Starting condition.
11/19	VII	500 H_2, 4,000 O_2, (4,500 O_2)*	Following single burst O_2 ingress.
11/19	VIII	n.d. H_2, 50 O_2, n.d. CO and CH_4	Following 130-minute purification.
11/20	IX	50 O_2, n.d. H_2, CO, CH_4	Starting condition.
11/20	X	3,400 H_2, 50 O_2, 40 CO, 60 CH_4	After 2 1/2 hours of H_2O injection with H_2 removal.

(1) Values are estimated from chromatograms, except where noted as ()* in which case they are estimated by mass balance calculations.

n.d. Not detectable. Below limit of detection for that constituent.

and additions to the HIL are in the monitoring systems. Two moisture monitors, a C.E.C. instrument with a P_2O_5 cell and a new Panametrics instrument (operating principle is based on Al_2O_3 sensor) have been added. The gas chromatograph system has been improved (1) by adding another column to resolve CO_2 and H_2O, (2) by adding another carrier gas, detector and column to increase H_2 sensitivity, and (3) by adding larger sample loops to improve overall sensitivity. The system now consists of two chromatographs, as described in Table 2-2. Chromatograph A, a dual column instrument with He carrier gas, will be used to measure the fixed gases shown and H_2O while chromatograph B, a single column instrument with N_2 carrier gas, will be used to measure H_2. The placement of the various monitors in the HIL are also shown in Figure 2-1.

After the modifications to the impurity injection and monitoring circuits were concluded, the loop test sections were installed. The materials for the first test run (described in detail in the previous progress report[2-1] are types H451, ATJ and PGX graphites in the form of 1/4-inch and 1/2-inch diameter tensile test specimens. The operating conditions for the first 500-hour exposure will be:

Maximum temperature	=	750°C
Helium flow rate	=	5.2 lbs/hr
Impurity level	=	100-200 ppmv H_2O, < 500 ppmv H_2.

The loop water level (100-200 ppmv at 1 atm.) is equivalent to 2-4 ppmv at 50 atmospheres (HTGR pressure). The exposure of these speci-

Table 2-2

HIL Gas Chromatographs

Chromatograph	Carrier Gas	Column Type	Gases Resolved	Sensitivity[1], ppmv
A	He	6-foot Molecular Sieve 5A	O_2	3
			N_2	4
			CO	10
			CH_4	5
	He	10-foot Porapak Q	CO_2	2
			H_2O	10
B	N_2	20-foot Molecular Sieve with D.C. 500	H_2	50[2]

(1) Minimum detectable limit.

(2) Estimated but not measured yet.

mens in the HIL has recently been started.

2.2 Oxygen Meter (H. Isaacs)

The start-up and operation of the HIL offered an opportunity to demonstrate the sensitivity of the electrochemical oxygen activity meter for the monitoring of the oxygen activity in helium over a wide range of impurity levels. The meter was highly responsive to all changes in the loop which influenced the oxygen activity including purification, reaction with graphite, reactions with the loop containment and impurity injections. These aspects are discussed below. The one major advantage of the meter was its rapid response to impurity changes. Determination by other monitoring methods required significantly longer periods before the changes could have been detected. The rapid response makes the oxygen activity monitoring technique attractive for the determination of sudden concentration changes which require rapid system responses.

The potential of the oxygen meter depends on the oxygen activity in the helium. When free oxygen is present in equilibrium with the helium the oxygen activity is equal to its partial pressure, and the magnitude of the potential is of the order of -0.1 volt. Figure 2-2 shows a calibration curve for the meter operating at 650°C with a Ag electrode and compares the theoretical curve with values obtained from gas chromatograph measurements following oxygen injection into the HIL. (See section 2.1 for the date 11/19). The plot is obtained from the Nernst equation, $E = \frac{RT}{4F} \ell n \, (P_{O_2}/0.21)$ where E is the potential, R is the gas constant, T the absolute temperature, F the Faraday

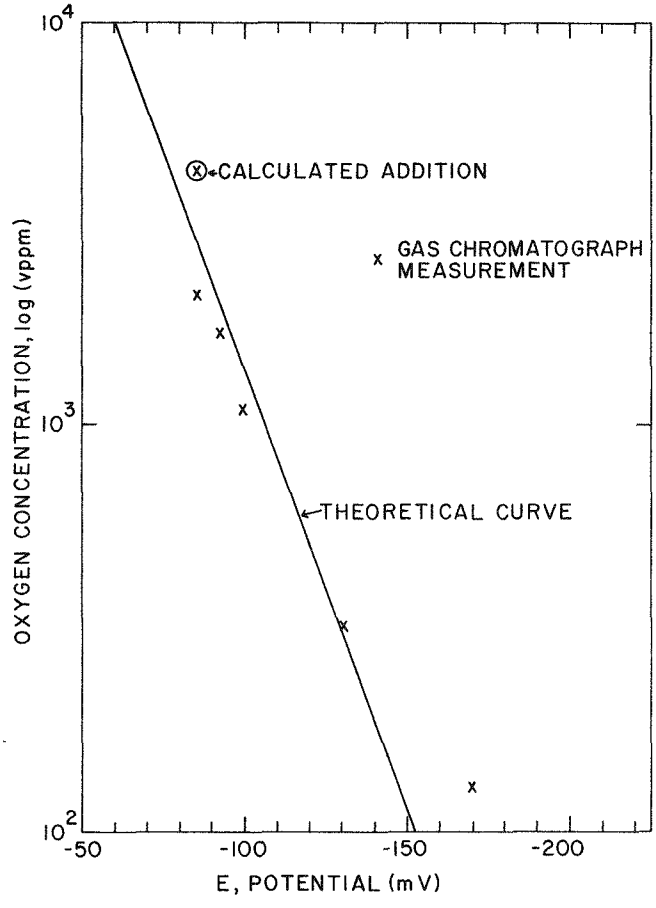

Figure 2-2. The calculated potentials of the oxygen meter at 650°C as a function of the oxygen partial pressure in atmospheres and as a function of the ratios of water to hydrogen and carbon dioxide to carbon monoxide.

constant, P_{O_2} the oxygen partial pressure and 0.21 is the oxygen pressure in air which acted as a reference electrode. Good agreement was observed at concentrations above 200 ppm oxygen. Below this concentration marked deviations were observed. These deviations could be a result of difficulties in the sensitivity of the gas chromatograph which have now been overcome, or as a result of the presence of H_2 or CO. At high H_2 concentrations (data obtained on 11/14) larger deviations were observed. These deviations arise from the different methods of determining oxygen. The gas chromatograph represents what concentrations are present in the loop while the oxygen activity meter, which was operated at 650°C allows the gases to react and approach thermodynamic equilibrium. Under these conditions the effective oxygen activity represents the oxygen remaining in the gas which had not reacted with hydrogen. This behavior is a disadvantage of the present meter with Ag electrodes at 650°C. At higher temperatures with a Pt electrode the meter would approach thermodynamic equilibrium more closely but deviate further from concentrations in the loop. However, the potential ranges observed with the meter were still low (below -300 mV) indicating the presence of free oxygen.

The response to free oxygen is clear with the meter because of the high oxygen activities. When the oxygen concentration is decreased to below the 1 ppm level the response of the meter to the oxgyen will be reduced and other impurities present, at or above the 1 ppm level, will begin to dominate the oxygen activity. For example,

if water and hydrogen were present the oxygen activity would depend on their ratio. This ratio can be used to calculate the expected oxygen activity. The calculated value indicates an expected potential of around -1 volt, far greater in magnitude than that indicated for the presence of oxygen. A similar conclusion would be reached considering CO and CO_2 to be present at concentrations significantly higher than that of oxygen. The potential expected from the ratio of CO and CO_2 would be relatively close to that for a given H_2/H_2O ratio. Figure 2-3 again shows a calibration curve for the meter but in this case over an extended potential range. This figure includes the potentials expected for ratios of P_{H_2O}/P_{H_2} and P_{CO}/P_{CO_2}. At any given potential, for example -0.7 volts, the figure shows that for equilibrium the oxygen partial pressure, the H_2/H_2O and the CO/CO_2 ratios would be about 10^{-14}, $10^{6.8}$ and $10^{7.9}$, respectively. The magnitudes of the numbers all indicate that the partial pressure of O_2, H_2 and CO would be present in extremely small concentrations. Under these conditions minor perturbations in the reaction sequence at the electrode would have a marked effect on these concentrations and the potential would vary rapidly. This behavior has been observed between potentials of about -0.3 and -0.8 volts where the rate of change was extremely rapid. In other words, in this range there is not sufficient concentration of potential controlling species to buffer the oxygen activity. This behavior has been observed after injection of oxygen or air.

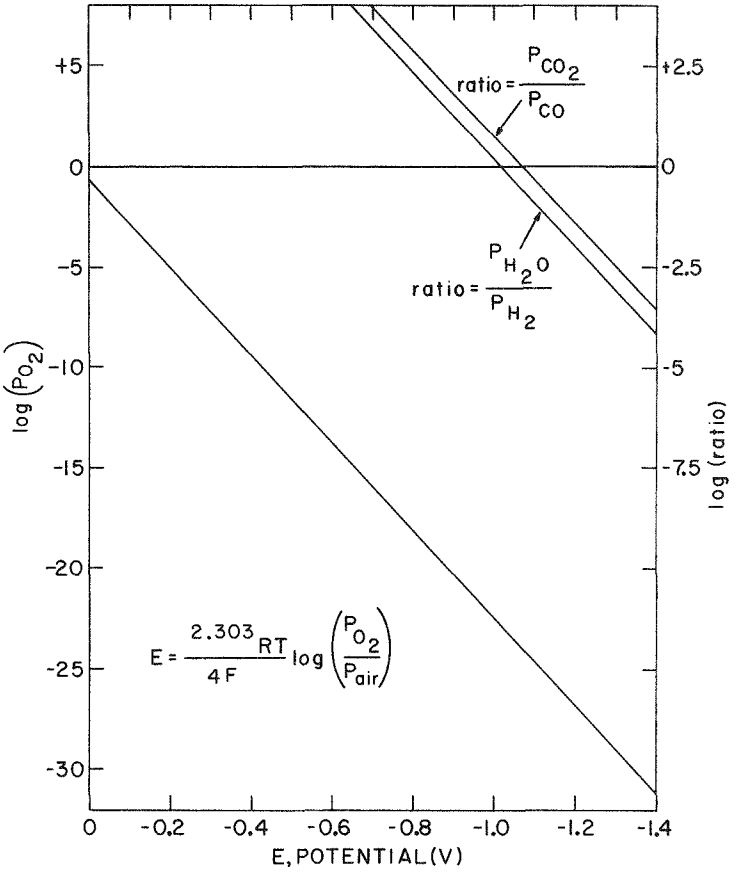

Figure 2-3. The comparison of the calculated potentials of the oxygen meter with the concentrations measured using the gas chromatograph.

On 11/19/75, when 100 cc or 4,300 ppm oxygen were injected the potential changed from -0.920 to -0.084. The rate of potential change was greatest when the potential changed from -0.800 to -0.200 mV as expected. When the oxygen reacted first with graphite and then with the loop walls the greatest rate of change was in the potential range of about -0.35 to -0.7 volts. During this run, while the oxygen reacted initially with the graphite at 550°C, the potential increased almost linearly with time at a rate of $-0.1 \pm 0.25 \times 10^{-5}$ volt/sec over the potential range of -0.085 to -0.130 volts. This range corresponds closely to an order of magnitude decrease in oxygen concentration (see Figure 2-2) from about 2,500 to 320 ppm.

If the rate of reaction of oxygen with graphite was first order, then the concentration or partial pressure (P_{O_2}) is given by:

$$P_{O_2} = P^{o}_{O_2} e^{-kt}$$

where t is time, $P^{o}_{O_2}$ is the initial oxygen partial pressure and k is the rate constant. Substitution into the Nernst equation for an oxygen concentration change from $P^{o}_{O_2}$ to P_{O_2} gives a potential difference:

$$E' = \frac{RT}{nF} \ell n \frac{P_{O_2}}{P^{o}_{O_2}} = - \frac{RT}{4F} kt.$$

This equation shows that for a first order reaction the rate of potential change is linear. Hence, over the oxygen concentration range given above the rate of reaction is first order and equal to

5.03×10^{-4} sec^{-1}. The rate constant was calculated for the graphite block and gave a rate of carbon oxidation of 1.5×10^{-4} $g/cm^2 - h^{-1} - atm^{-1}$. This value is compared to a rate of 4.4×10^{-3} $g/cm^2 - h^{-1} - atm^{-1}$ calculated from formulations used in section 7.5. The agreement is reasonable considering the variation in observed rates of graphite oxidation. A closer agreement was obtained with air oxidation of H451 graphite which gave a rate of 1.3×10^{-4} $g/cm^2 - h^{-1} - atm^{-1}$.

After the linear change in potential with time the rate of change increases. This would correspond to an increase in the rate constant. For graphite/oxygen reactions a decreased rate constant would be expected as the concentration of oxygen decreased because of the buildup of inhibiting reaction products. The increased rate was attributed to other reactions in the loop, for example with the walls or metal components in the system. This was clearly demonstrated when the graphite tank was valved out of the system and helium flowed through the bypass circuit; the potential still continued to change. The relative areas of metal surface were also changed which was reflected in the rate of variation in potential.

During the course of this work, one oxygen meter was found to be defective because the electrolyte had cracked. The potential of the meter showed a much higher oxygen activity than was expected. This level decreased as the flow rate increased because of the dilution of the oxygen leaking through the crack. Under normal operation the response to the flow rate is small.

2.3 Fuel Hydrolysis and Oxidation (D. Chandra)

A shipment of bare weak acid resin kernels was received from the Oak Ridge National Laboratory during this quarter. These particles were not pre-exposed to air and were made with natural uranium. Five different batches of particles were received, with 0%, 25%, 50%, 75% and 100% conversion, respectively.

A dry inert atmosphere glove box was set up and put into operation. This is necessary because the weak acid resin kernels acquired are pyrophoric and unstable in air. Great care, therefore, is necessary in handling these particles prior to and during the experimental run. The glove box was exposed to air before its procurement. Furthermore, a number of accessory components had to be repaired and checked. The glove box is now working properly. The seal of the fuel container will be broken within the glove box.

A request was made to the General Atomic Company for a batch of current design VSM coated UC_2 fuel particles. During a visit to GA on October 16 and 17, 1975, discussions were held with GA personnel to establish the availability of current design HTGR UC_2 fuel particles, for which GA is the only known source. During those meetings, specific batches of fuel particles were identified and the list of batch numbers was provided to us to be included in our formal request.

Some additions were made in our experimental plans on the whole fuel hydrolysis/oxidation area. Initially some atmosphere reactivity experiments on the weak acid resin (W.A.R.) kernels will be carried out to permit a preliminary comparison with the experiments

on atmospheric reactivity carried out at Oak Ridge[2-2] and thus provide an initial assessment of our experimental procedures.

Atmospheric reactivity of the W.A.R. fuel kernels is important from the safety point of view since it has been reported that exposure of the fuel to water vapor following conversion produced deleterious effects in the kernel[2-3]. It produces roughening of the kernel surface and while this does not directly produce fuel dispersion into the buffer it does contribute to uranium redistribution when SiC coating is subsequently applied to the BISO particle.

References

2-1 HTGR Safety Evaluation Division Quarterly Progress Report, July-September, 1975, BNL-50479.

2-2 Gas-Cooled Reactor Programs Annual Progress Report, period ending December 31, 1973, ORNL-4975.

2-3 HTGR Base Program Monthly Progress Report, June 1975, ORNL-GCR-B.75-3.

3. Task Area III - Rapid Graphite Oxidation

3.1 Chemical Analysis of Graphite (A. Romano)

A log of ATJ graphite has been sectioned and sampled at 200 random locations. The samples are presently being analyzed for the impurities discussed in the previous progress report[3-1] by the standard emission spectrographic method. With the reporting of the results of the analysis of these 200 samples, the statistical graphite chemistry work will be limited to generic reactor safety problems.

3.2 Graphite Oxidation (H. S. Isaacs)

The Cahn recording microbalance has been set up for oxidation of graphite. An experiment was carried out with an H451 sample in air at 550°C for 20 hours to check the weight loss with standard methods. The recording balance gave a weight change of 15.2 mg while the standard method gave 14.33 mg. The causes for this difference are being investigated.

The rate of weight change calculated for this run was about 1.3×10^{-4} $g/cm^2\text{-}h^{-1}\text{-}atm^{-1}$. This value is in excellent agreement with the rates obtained during oxygen reaction with H451 graphite during HIL operation as described in section 2.2.

3.3 Investigation of the Role of Iron in Catalytic Oxidation of Graphite Using Mössbauer Spectroscopy (D. Chandra, H. Isaacs)

An experimental program is currently in progress to study the influence of iron on the oxidation behavior of ATJ and PGX graphites. These two graphites are HTGR core support block and post materials. Mössbauer spectroscopy is being used to study the change in chemical form of iron with progressive oxidation in an H_2O-He mixture and following heavy oxidation, progressive reduction in hydrogen. A review of Mössbauer effect and its application can be obtained from Wertheim[3-2].

Mössbauer effect is highly sensitive to the local electronic environment of the absorbing nucleus. The Mössbauer nuclide under consideration here is ^{57}Fe, which has a natural 2.12% abundance. When the ^{57}Fe nucleus is in a ferromagnetic environment, a six line resonance absorption pattern is seen, with the separation between the lines proportional to the magnetic hyperfine field at the nucleus. Thus the pattern for natural α-iron is a six line pattern. Iron compounds, for example oxides, will correspond to a different chemical environment around the ^{57}Fe nucleus. Thus the magnetic hyperfine field at the nucleus will change leading to an altered separation between the lines. For non-ferromagnetic compounds, only a single line spectrum will be seen. The samples to be studied using Mössbauer spectroscopy are generally (though not exclusively) introduced as the absorbers. The emitter is prepared by diffusing the 270-day

half-life ^{57}Co radioactive isotope into a matrix material; in this case, copper. The ^{57}Co decays into an excited state of the ^{57}Fe nucleus which in turn emits a 14.4 keV γ-ray photon, decaying into the ^{57}Fe ground state in the process. This 14.4 keV γ-photon in turn excites the ^{57}Fe nucleus in the absorber from the ground to the excited state when the chemical/magnetic environments of the nuclei are identical in the emitter ("source") and the absorber. This forms the basis of the technique (resonant absorption). If the chemical/magnetic environments in the source and the absorber are not identical, then differences between excited and ground states will be different in each and resonant absorption ordinarily will not take place. In this case, a doppler shift can be introduced in either the source or the absorber to compensate for the difference in chemical environment. The Mössbauer spectrum, therefore, is plotted as the fraction of the 14.4 keV γ-photons transmitted through the absorber against the doppler velocity.

Figure 3-1a shows the metallic iron spectrum, Figure 3-1b shows the Fe_2O_3, 3-1c the Fe_3O_4, and 3-1d the FeO_x (Wustite) spectrum. There are large differences between their spectra, and it is possible to differentiate one spectrum from the other. The "resolution" of detecting oxide formation is relatively good and a 0.1 to 0.5% change in the iron chemical species can be detected; this refers to a natural iron level of 4.44 mg/cm^2 of absorber cross-sectional area.

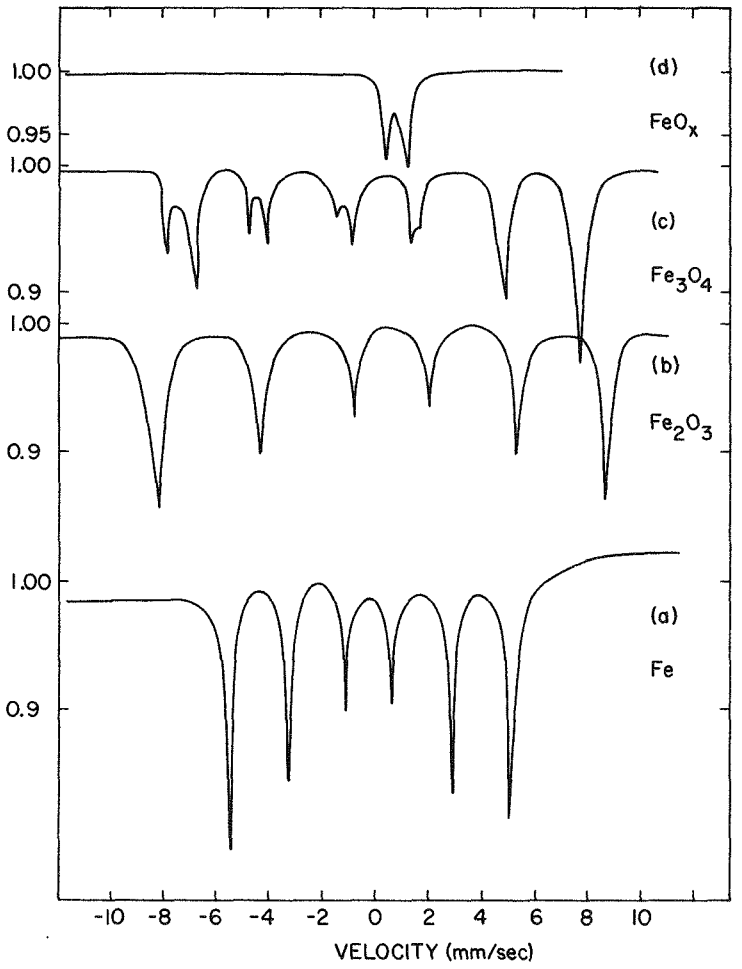
1.00
0.95
1.00
0.9
1.00
0.9
1.00
0.9
(d)
FeO$_x$
(c)
Fe$_3$O$_4$
(b)
Fe$_2$O$_3$
(a)
Fe
-10 -8 -6 -4 -2 0 2 4 6 8 10
VELOCITY (mm/sec)

Figure 3-1.

Figure 3-2a shows the spectrum obtained from an as received PGX graphite sample. This six line spectrum is identical to that shown in Figure 3-1a earlier, and therefore the iron (usually between 0.1 to 1% in the graphite) must then be present in a metallic form.

Figure 3-2b and 3-2c show progressive changes in the spectrum of this sample following oxidation in a flowing gas mixture of 2% H_2O in helium at 650°C. The metallic iron peaks increasingly broaden with oxidation and even after 2 hours, very small oxide peaks at high velocity are discerned. With progressive oxidation these oxide peaks increase in intensity. The spectra shown in Figure 3-2 were obtained from the center of the sample. The oxide peak intensity was found to change somewhat from one end of the sample to the other. Figure 3-3a shows the spectrum of a sample oxidized for 2 weeks at 650°C in a 2% H_2O-He mixture. The entire iron is present as oxides, primarily as Fe_3O_4. Figure 3-3b shows the spectrum of this sample after being exposed to a hydrogen-helium mixture for 5 hours, and the iron was found reduced to the metallic state.

These results point to the applicability of Mössbauer spectroscopy in determining depth of reaction in these graphites. In the spectra shown in Figure 3-2 above, assuming the iron is homogeneously distributed throughout the sample, the ratio of iron atoms present as oxides to iron atoms present as metal may then permit an estimation of the depth of oxidation. Efforts are now being directed to this area.

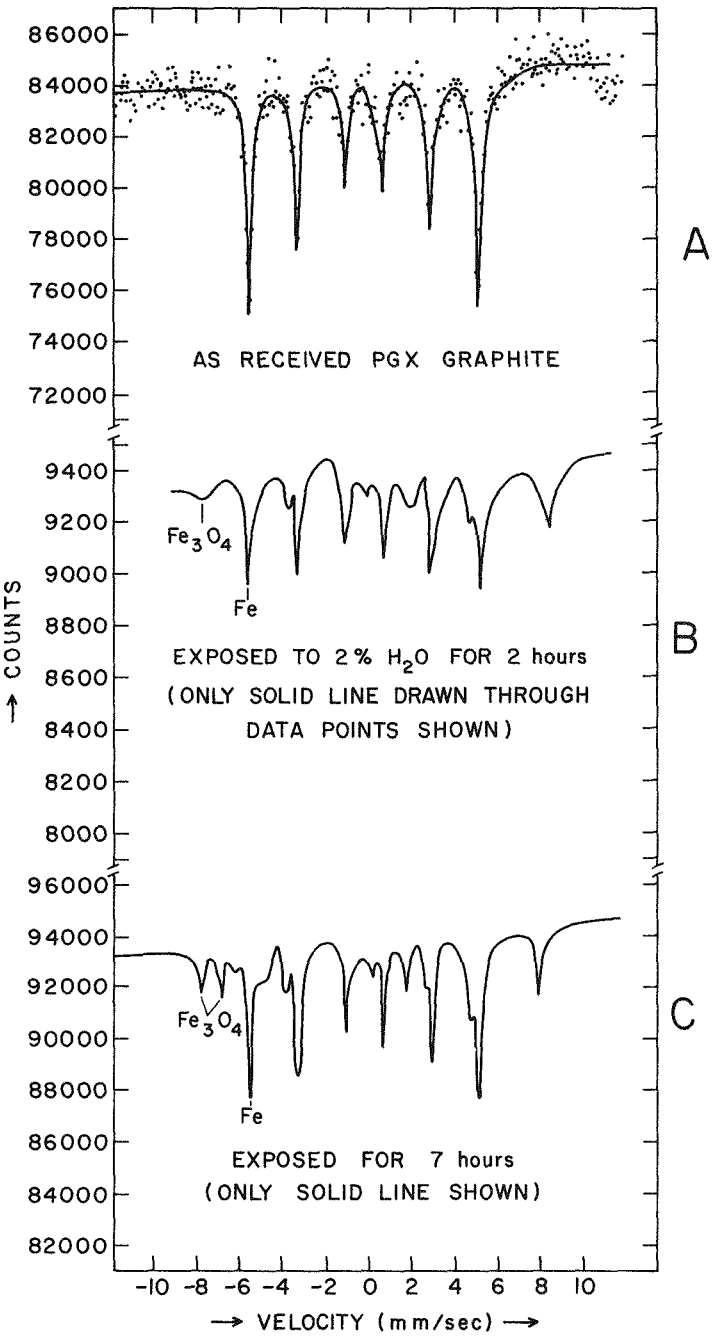
86000
84000
82000
80000
78000
76000
74000
72000
A
AS RECEIVED PGX GRAPHITE
9400
9200
9000
8800
8600
8400
8200
8000
Fe3O4
Fe
B
EXPOSED TO 2% H2O FOR 2 hours
(ONLY SOLID LINE DRAWN THROUGH
DATA POINTS SHOWN)
COUNTS
96000
94000
92000
90000
88000
86000
84000
82000
Fe3O4
Fe
C
EXPOSED FOR 7 hours
(ONLY SOLID LINE SHOWN)
-10 -8 -6 -4 -2 0 2 4 6 8 10
VELOCITY (mm/sec)

Figure 3-2.

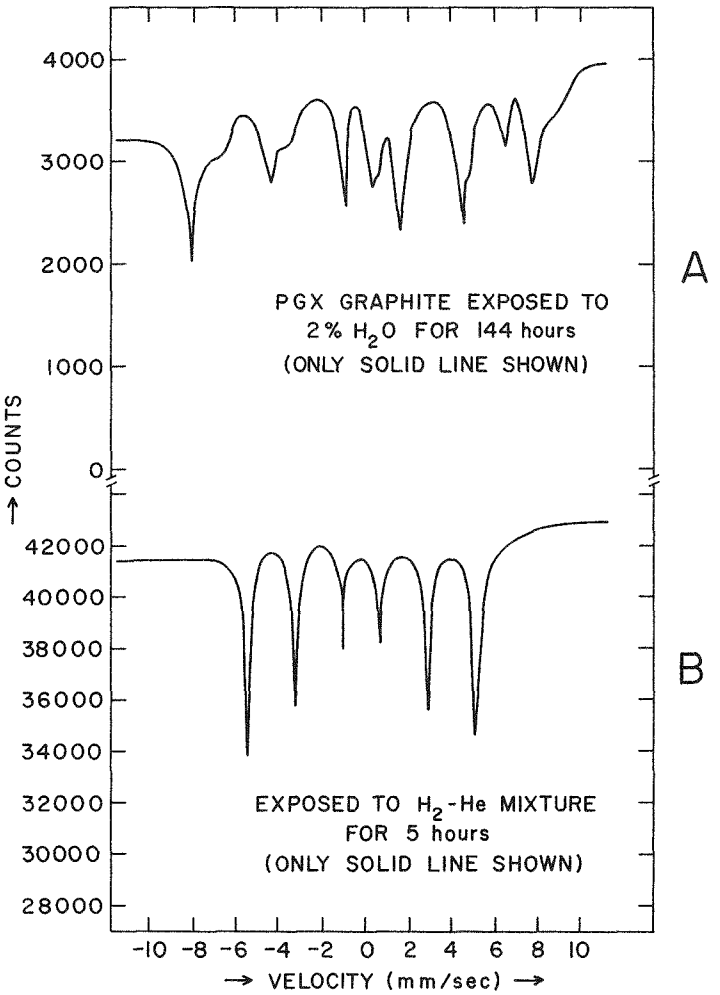
4000
3000
2000
1000
0
PGX GRAPHITE EXPOSED TO
2% H_2O FOR 144 hours
(ONLY SOLID LINE SHOWN)
A
→ COUNTS
42000
40000
38000
36000
34000
32000
30000
28000
B
EXPOSED TO H_2-He MIXTURE
FOR 5 hours
(ONLY SOLID LINE SHOWN)
-10 -8 -6 -4 -2 0 2 4 6 8 10
→ VELOCITY (mm/sec) →

Figure 3-3.

Work is in progress to develop these results into the establishment of a systematic technique to determine the depth of oxidation and to understand the role of iron in graphite oxidation.

References

3-1 HTGR Safety Evaluation Division Quarterly Progress Report, July-September, 1975, BNL-50479.

3-2 G. K. Wertheim, The Mössbauer Effect; Principles and Applications, Academic Press, New York, 1964.

3-3 "Evidence for Quadrupole Interaction of Fe^{57m} and Influence of Chemical Binding on Nuclear Gamma-Ray Energy," Phys. Rev. Ltrs. 4, 412 (1960).

4. Task Area IV - Structural Evaluation (M. Reich, P. Bezler, B. Koplik, J. R. Curreri, T. Y. Chang, L. Lasker, H. Goradia, F. Kautz)

The work carried out by the Structural Analysis Group during this report period can be categorized into the areas of Core Seismic Response and PCRV and Liner.

4.1 Core Seismic Response

As was shown in the previous quarterly report (July-September 1975) the horizontal dynamic response of the multi-mass model could be accurately predicted by a reduced mass model. During the present report period the horizontal core model was further modified to include the entire core of the HTGR.

Figure 4-1 depicts the actual cross-section of the core. The divisions shown in the figure indicate how the masses in the new model are lumped. Furthermore, as shown in the schematic representation, Figure 4-2, the total mass of the core is represented by a seven mass model where the masses are unequal. The model is symmetric and consistent with the true core support block boundaries. Masses m_1 and m_7 represent the core reflector blocks. The other masses, m_2 through m_6, represent the internal components of the core. The model includes the interelemental damping CI, the ground damping GCI, the material stiffness between the various core elements K_i, and the appropriate clearances. The reflector blocks are connected by an elastic link with an adjustable gap. This simulates the true reactor configuration in that the actual reflector blocks can only move a short distance radially inward before they exhaust their cir-

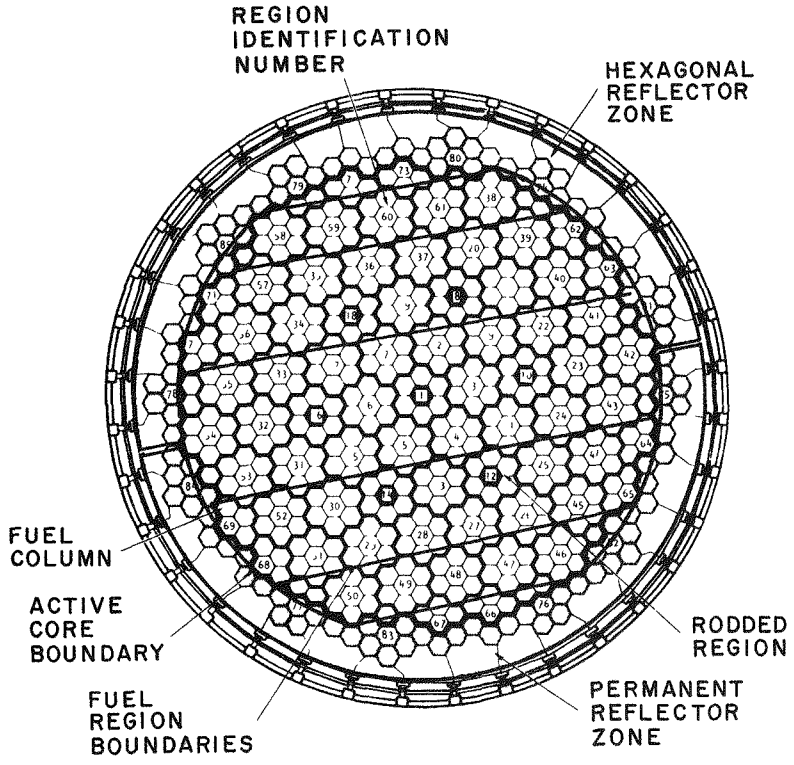

Figure 4-1. Core subdivisions 7 mass model.

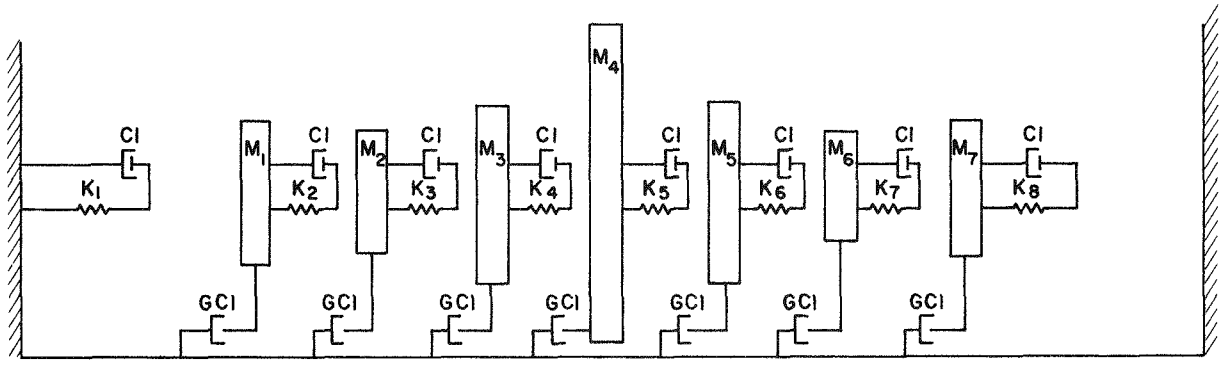

Figure 4-2. 7 mass model unequal mass distribution.

cumferential clearance and "lock-up." A modification of the horizontal array code, OSCIL, was necessary in order to implement this analysis.

Computer runs were made using the modified code with various reflector block gaps. The extent of the variations covered the full range of possibilities from zero gap to a very large gap. In all cases, the input was a sine wave with a 1-inch amplitude. Figure 4-3 shows the time-history response of the seven mass model in which the gap is sufficiently large so that closure never occurs. This is essentially the same case as was shown in the previous quarterly report as Figure 4-3. The major difference between the two models is that the present model is for the whole core with unequal mass distribution while the earlier model was for a single slice across the diameter with equal mass distribution.

As was expected the two response plots are quite similar with the first frequency of maximum response occurring at about 2.52 rad/sec in each case. This is the frequency at which the maximum boundary forces are developed.

Figure 4-4 shows the time-history response of the same model with a rigid link connecting the two reflector blocks (zero gap). In this case the frequency of maximum response occurs at 2.70 rad/sec, a value slightly higher than that for the unrestrained case. Other cases with gaps ranging from 0.2 to 2.0 inches showed that the frequency of maximum response does not change appreciatively from the value of 2.52 rad/sec.

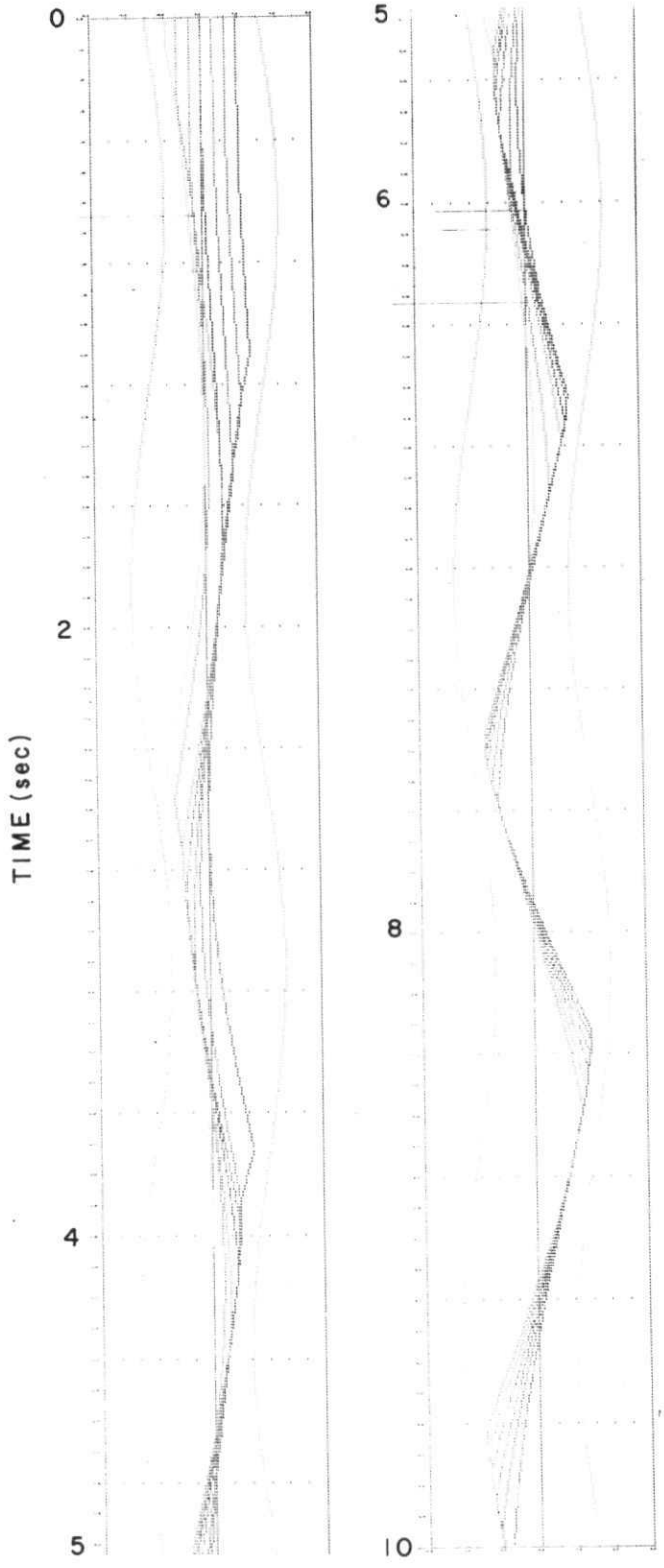

Figure 4-3. 7 mass model with reflector blocks unconstrained, first resonant mode.

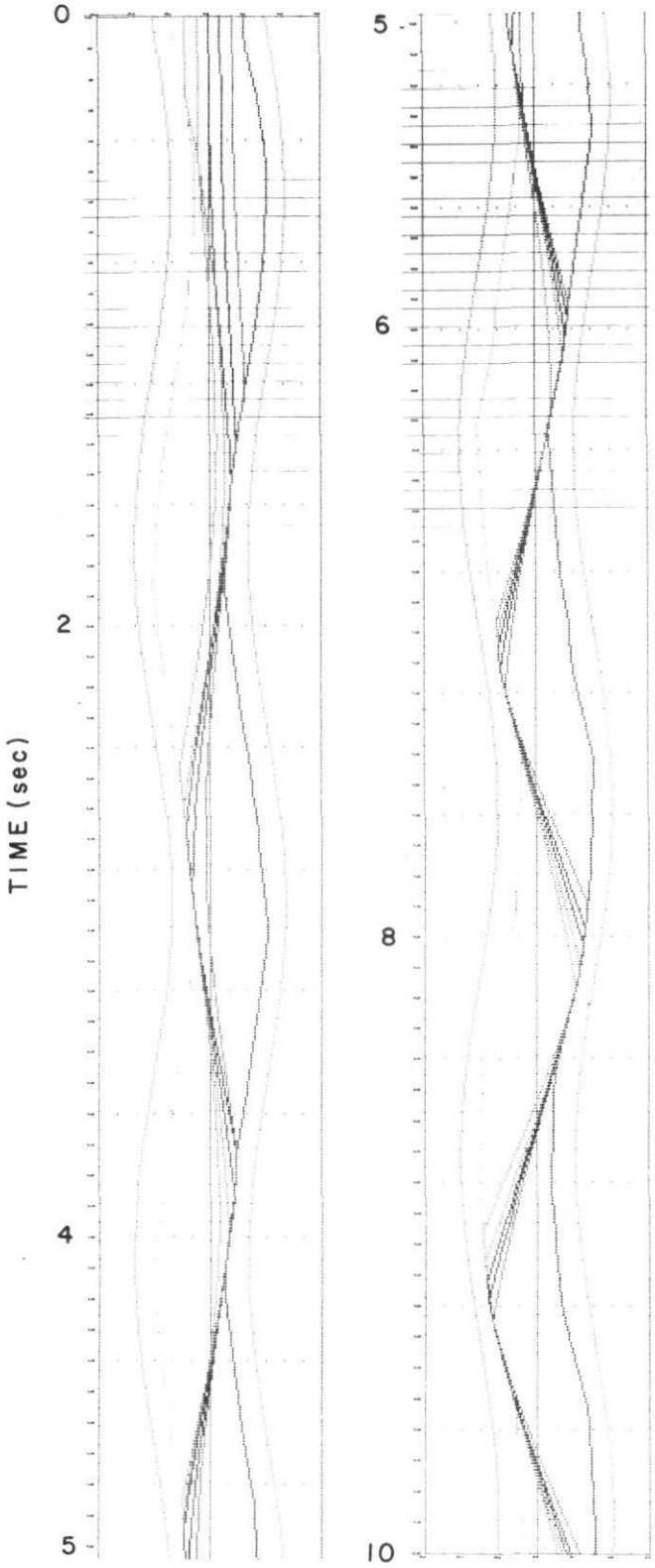

Figure 4-4. 7 mass model with reflector blocks rigidly connected, first resonant mode.

There were, however, significant changes in the second mode response characteristics for each of the cases with different gap sizes. For all the previous runs where the reflector blocks were mutually unconstrained the second mode natural frequency was well above the highest significant frequency of the earthquake spectrum. As the size of the gap is decreased the second mode frequency is lowered. For the fully constrained case (zero gap) the second mode occurs at 4.02 rad/sec. The time-history response for this mode is shown in Figure 4-5. As a comparison, if the gap is increased to 1 inch, the second mode frequency is increased to 12.9 rad/sec.

There are, therefore, two secondary effects which produce frequencies of maximum response. One of these effects was described in previous reports as the first subharmonic of the fundamental frequency which occurs at twice the fundamental frequency. For the fundamental frequency of 2.52 rad/sec the first subharmonic was observed to be 5.0 rad/sec. In the present case another effect is demonstrated as the second mode of vibration is revealed. The magnitude of the second mode depends upon the size of the gap. For the same fundamental frequency of 2.52 rad/sec a second mode is excited ranging from 4.02 rad/sec for zero gap size up to 40 rad/sec as the gap increases.

The horizontal array shake tests were carried out with a seven block array as shown in Figure 4-6. The tests were recorded with high speed motion picture equipment. An evaluation of the filmed results is in process. The model did exhibit the key characteristics

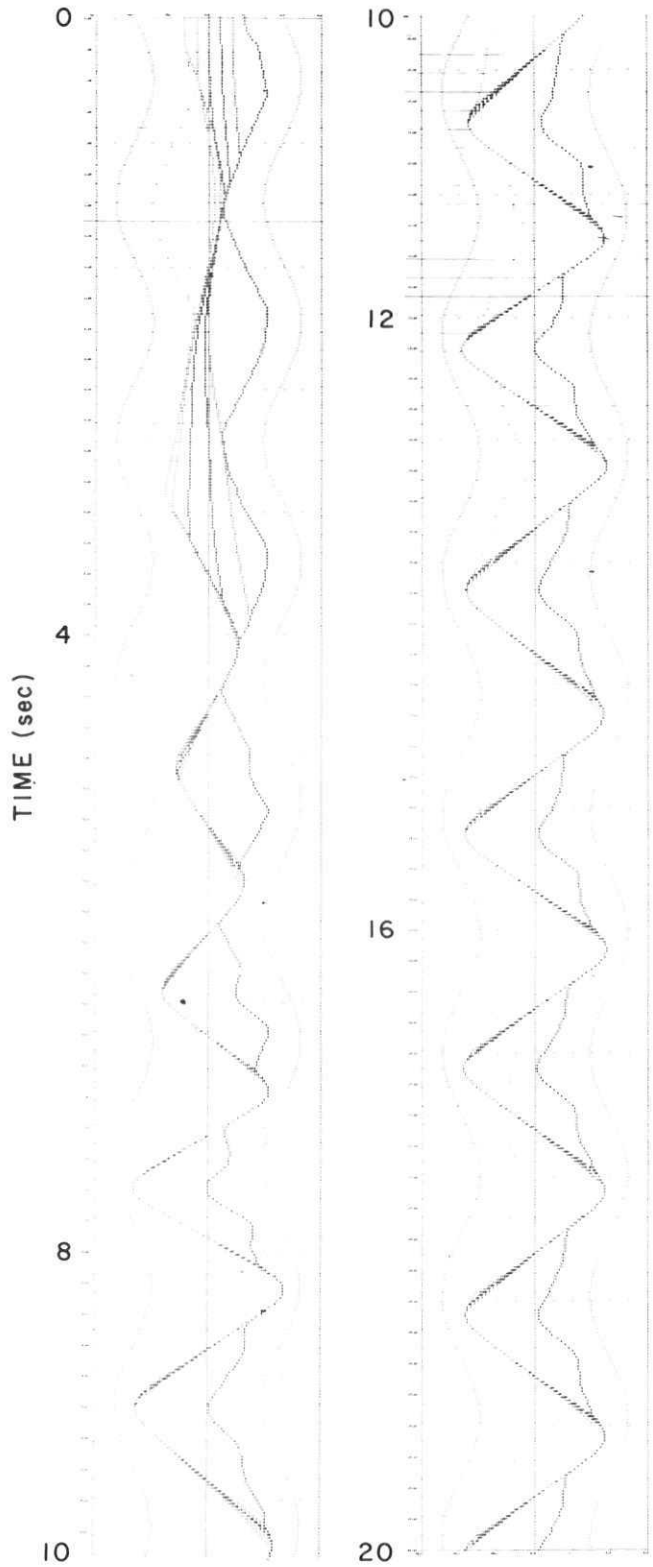

Figure 4-5. 7 mass model with reflector blocks rigidly connected, second resonant mode.

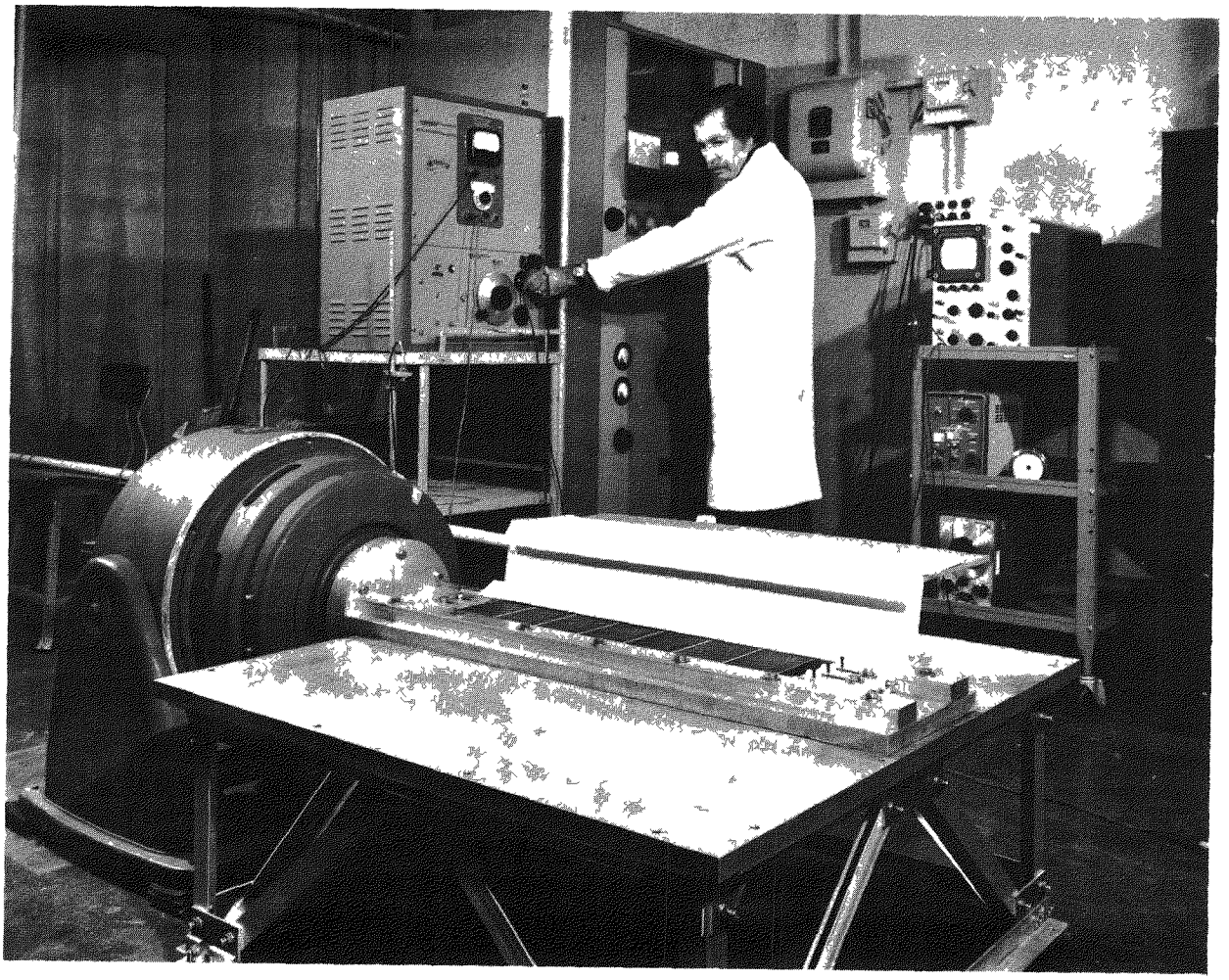

Figure 4-6.

of a hardening non-linear system. The jump phenomenon was distinctly apparent, the amplitude of motion and noise increased with increased drive frequency, then suddenly dropped to essentially zero at a distinct reproducible frequency. In sweeping down, the jump from a small response to a noticeably larger response occurred at a lower frequency than the drop frequency as was expected. Trial duplication runs with the OSCIL code corraborated the force levels developed during test, estimates of test forces being made by noting end spring deflections and then comparing them with predicted results.

The development of the "n" element vertical array code, OSVERT, is complete. It has been tested with up to 10 elements and found to operate correctly. The code predicts the horizontal, vertical and rotational time response of an "n" element stack subjected to simultaneous horizontal and vertical ground excitations. It produces both a digital and graphical time-history output of the displacements for each element. To date, only program test runs have been made with the code.

4.2 PCRV and Liner

Substantial progress has been made during the past few months in the development of a computer code to handle all types of behavior that could occur throughout the design life of the PCRV. Unlike GA's safe crack and creep codes which are two dimensional plane or axisymmetric and use a simple triangular constant stress finite element, the present code is three dimensional and is based on the more versatile isoparametric finite elements developed during the

last few years. Some of the important features included in the current code are:

1. Failure criteria that accounts for either biaxial or triaxial tensile cracking and compressive crushing of concrete. The failure criteria adjusts for reductions in tensile strength due to compression in the other directions and for the increase in the compressive strength due to either biaxial or triaxial compression in the other directions at a particular point of the concrete structure.

2. Partial cracking or crushing of elements is permitted.

3. Unloading in compression and tension, as well as reloading in compression and tension is also possible with this method.

4. Both short term shrinkage, as well as long term constant or variable load concrete creep are accounted for in terms of temperature, stress-strength ratio, and compressive stresses.

5. Prestressing cable force losses are evaluated as functions of long term relaxation, fraction, and the elastic and inelastic deformations inherent in the structure.

6. Steel component inelastic behavior is accounted for in terms of a bilinear stress-strain relationship together with an equivalent effective stress and strain that relates uniaxial behavior with the biaxial or triaxial state. The program uses an initial strain condition to specify the stress state for initial plastic deformation, a flow rule that allows for the determination of plastic strain increments at each of the steps in the loading history, and a hardening rule to provide for modifications occurring to the yield sur-

face during plastic flow. A large deformation and buckling failure routine is also being worked on. It incorporates an approach that would account for a fracture mechanics type of evaluation for liner failure.

Figures 4-7 and 4-8 depict results of a sample run consisting of a 30^{o} section of a 1160 MW electric plant potted vessel with a $250^{o}F$ temperature at the linear concrete interface and a cavity pressure of 770 psig. It needs to be emphasized that although substantial progress has been made, this effort is only in its early stages and quite a bit of work still needs to be carried out to make this code an effective, versatile, simple and relatively inexpensive tool for large potted type PCRV analysis.

As an extension of the PCRV analysis method, the development of a non-linear dynamic analysis procedure has been undertaken. The code has all the capabilities of the static PCRV code and in addition includes dynamic failure analysis capabilities.

For handling the material non-linearities, we are using an iterative method. With this scheme, the structure is analyzed several times during a time step for the same applied load. At the end of each solution cycle for a particular time step, the unbalanced load that cannot be resisted by the structure (due to its non-linear behavior) is calculated and redistributed over the structure by the next iteration cycle. The structure is then analyzed successively for the applied load at the particular time step until convergence for that time step is achieved. The same procedure is followed for the

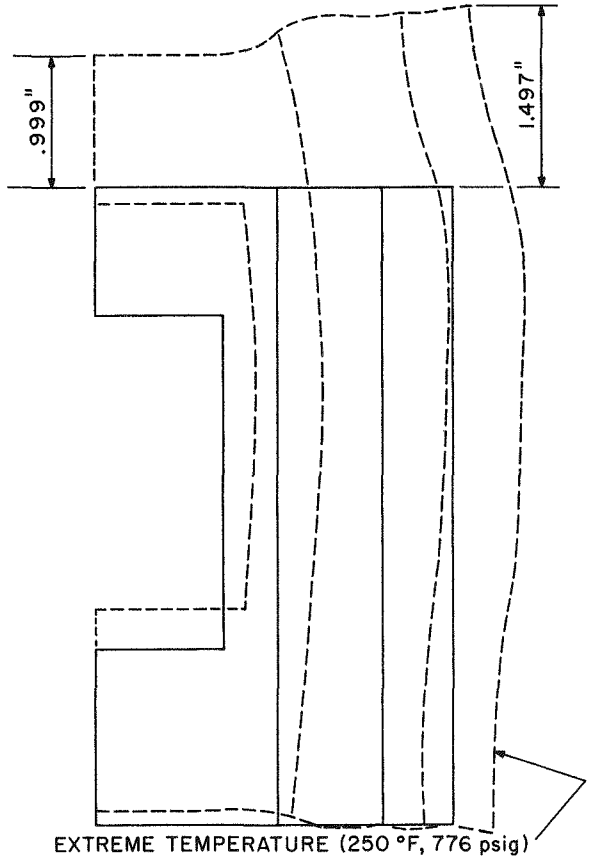

Figure 4-7. PCRV displacements for extreme temperature.

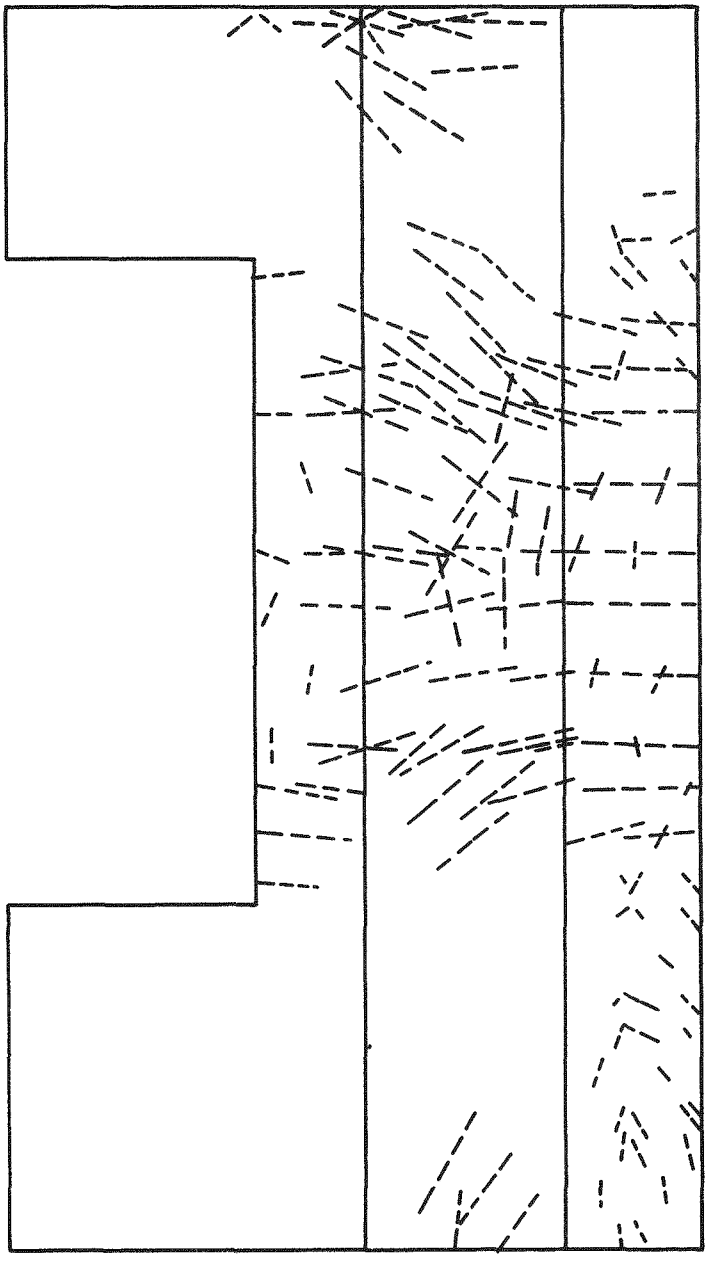

Figure 4-8. Concrete cracks for extreme temperature (250°F).

next time step, and so on.

The equations of motion for a multi-degree-of-freedom system can be written as:

$$\underset{\sim}{M}\ddot{\underset{\sim}{U}} + \underset{\sim}{C}\dot{\underset{\sim}{U}} + \underset{\sim}{K}\underset{\sim}{U} = \underset{\sim}{P} \tag{1}$$

or, more conveniently:

$$\underset{\sim}{M}\ddot{\underset{\sim}{U}} = \underset{\sim}{P}_E - \underset{\sim}{P}_I \tag{2}$$

where $\underset{\sim}{M}$ = mass matrix, $\underset{\sim}{C}$ = damping matrix, $\underset{\sim}{K}$ = stiffness matrix, $\underset{\sim}{U}$ = displacement vector, $\dot{\underset{\sim}{U}}$ = velocity vector, $\ddot{\underset{\sim}{U}}$ = acceleration vector, $\underset{\sim}{P}_E$ = consistent external forces and $\underset{\sim}{P}_I$ = consistent nodal forces due to internal stresses = $\int \underset{\sim}{B}^T \underset{\sim}{\sigma} dV$.

As an alternate form Equation (2) can be written as:

$$\dot{\underset{\sim}{U}} = \underset{\sim}{V} \tag{3a}$$

$$\underset{\sim}{M}\dot{\underset{\sim}{V}} = \underset{\sim}{P}_E - \underset{\sim}{P}_I \tag{3b}$$

Solving Equation (2) in this form is known as the "state variable approach." The direct time integration technique applied to Equations (3) is a variation of the trapezium scheme which incorporates "staggered" time integration scales, i.e., the time integration scale for the computation of the $\underset{\sim}{V}$'s is shifted by $\frac{\Delta t}{2}$ relative to the time integration scale for the computation of the $\underset{\sim}{U}$'s. We first develop the solution strategy in terms of the "conventional" trapezium scheme for time integration, i.e., with the same time integration scale for the computation of both the $\underset{\sim}{V}$'s and $\underset{\sim}{U}$'s. After substantial derivation and substitution it can be shown that the equations respectively for the conventional and staggered time integration schemes for the unknown time vectors at time t_{n+1} are respectively:

$$\underset{\sim}{U}_{n+1} - \frac{\Delta t}{2}\,\underset{\sim}{V}_{n+1} = \underset{\sim}{U}_{n} + \frac{\Delta t}{2}\,\underset{\sim}{V}_{n}$$

$$\underset{\sim\sim}{MV}_{n+1} = \underset{\sim\sim}{MV}_{n} + \frac{\Delta t}{2}\,(\underset{\sim}{P}_{E,n+1} + \underset{\sim}{P}_{E,n}) - \Delta t\,\underset{\sim}{P}_{I,n} - \frac{\Delta t}{2}\,(\iiint \underset{\sim}{B}^{T}\,\Delta\underset{\sim}{\sigma}\,dV) \tag{3c}$$

and

$$\underset{\sim}{U}_{n+1} = \underset{\sim}{U}_{n} = \Delta t \underset{\sim}{V}_{n+\frac{1}{2}}$$

$$\underset{\sim\sim}{MV}_{n+\frac{3}{2}} = \underset{\sim\sim}{MV}_{n+\frac{1}{2}} + \Delta t\,\underset{\sim}{P}_{E,n+1} - \Delta t\,\underset{\sim}{P}_{I,n} - \Delta t\,(\iiint \underset{\sim}{B}^{T}\,\Delta\underset{\sim}{\sigma}\,dV) \tag{3d}$$

With respect to the incremental stresses for the non-linear material problem, incorporated with the techniques above, the non-linear stress-strain relationship is defined by the following rate equation:

$$d\underset{\sim}{\sigma} = \underset{\sim}{D}\,d\underset{\sim}{\varepsilon}$$

where $\underset{\sim}{D}$ = material rigidity matrix, $\underset{\sim}{\varepsilon}$ = strain vector and $\underset{\sim}{\sigma}$ = stress vector. The incremental stresses are obtained by the integration:

$$\Delta\underset{\sim}{\sigma} = \int_{\underset{\sim}{\varepsilon}_n}^{\underset{\sim}{\varepsilon}_n + \Delta\underset{\sim}{\varepsilon}} \underset{\sim}{D}\,d\underset{\sim}{\varepsilon} \tag{4}$$

Using the Crank-Nicholson numerical integration scheme to evaluate the integral, we obtain:

$$\Delta\underset{\sim}{\sigma} = \underset{\sim}{\sigma}_{n+1} - \underset{\sim}{\sigma}_{n} = [\theta \underset{\sim}{D}_{n} + (1 - \theta)\,\underset{\sim}{D}_{n+1}]\,\Delta\underset{\sim}{\varepsilon} \tag{5}$$

where $\underset{\sim}{D}_n$ = rigidity matrix evaluated at $\underset{\sim}{\sigma}_n$, $\underset{\sim}{D}_{n+1}$ = rigidity matrix evaluated at $\underset{\sim}{\sigma}_{n+1} = \underset{\sim}{\sigma}_n + \Delta\underset{\sim}{\sigma}$. Iteration is required, therefore, to solve for $\underset{\sim}{D}_{n+1}$ when $\underset{\sim}{D}$ is a function of $\underset{\sim}{\sigma}$.

Equation (5) is an approximate "correct" expression for the stress increment. A choice of $\theta = 1$ corresponds to the Euler method:

$$\Delta\underset{\sim}{\sigma} = \underset{\sim}{D}_{n}\,\Delta\underset{\sim}{\varepsilon} \tag{6}$$

and a choice of $\theta = 0$ corresponds to the backward difference method

$$\Delta\underset{\sim}{\sigma} = \underset{\sim}{D}_{n+1}\,\Delta\underset{\sim}{\varepsilon} \tag{7}$$

We express $\Delta\underset{\sim}{\sigma}$ as:

$$\Delta\underset{\sim}{\sigma} = \Delta\underset{\sim}{\sigma}^* - \Delta\underset{\sim}{\sigma}_C \tag{8}$$

where

$$\Delta\underset{\sim}{\sigma}^* = \underset{\sim}{D}^* \Delta\underset{\sim}{\epsilon}. \tag{9}$$

$\underset{\sim}{D}^*$ is a specified regidity matrix and $\Delta\underset{\sim}{\sigma}_C$ is the imbalance in the incremental stress, or the "correction" needed to establish a balance between $\Delta\underset{\sim}{\sigma}$ (the approximate "correct" incremental stress) and $\Delta\underset{\sim}{\sigma}^*$ (computed with the assumed rigidity matrix). Using Equations (5) and (9), $\Delta\underset{\sim}{\sigma}_C$ can be expressed as:

$$\Delta\underset{\sim}{\sigma}_C = [\underset{\sim}{D}^* - \theta\underset{\sim}{D}_n - (1 - \theta)\ \underset{\sim}{D}_{n+1}]\ \Delta\underset{\sim}{\epsilon} \tag{10}$$

where for $\Delta\underset{\sim}{\epsilon}$ we can use:

$$\Delta\underset{\sim}{\epsilon} = \underset{\sim}{B}\ (\underset{\sim}{U}_{n+1} - \underset{\sim}{U}_n). \tag{11}$$

A more detailed description of the computational procedure combining the staggered time integration method with cases involving material non-linearity will be presented at a later date.

5. Task Area V - Materials

The work in this program area covers four groups of materials: (1) metals, (2) graphites, (3) PCRV, and (4) other materials, which include control rod and thermal barrier insulation. Objectives are to assess and review the state of the art, to identify the critical areas pertinent to HTGR safety, and initiate an experimental program to obtain required data.

Literature surveys are currently progressing to assess the state of the art in metals, graphite and PCRV technology. A major part of this work will be to analyze available materials property data and present design curves for safety-related analytical studies.

Equipment for tensile, creep, fatigue, and creep-fatigue testing is currently being evaluated for procurement to expand the capability of the mechanical testing laboratory. When this is received, testing will be performed in simulated normal and off-normal HTGR helium conditions. Additional equipment for pre-exposing materials in helium, prior to testing, is also being constructed.

As part of the materials program, a subcontract has been awarded to the Aerospace Corporation to evaluate fracture mechanisms in various graphites.

5.1 Metal and Graphite Testing (J. Chow, P. Soo)

Two of the three fatigue machines are currently inoperative because of oil leakage in the hydraulic systems and faulty electronics in one control console. Since the lack of available capital equip-

ment money has prevented any repairs from being conducted the entire experimental effort is currently centered on a single machine. It is anticipated, however, that capital equipment money will very shortly become available, at which time repairs will be made and additional fatigue and creep machines ordered (see previous quarterly progress report).

A sufficient quantity of materials is being purchased as a base for a long-term program. Alloys currently being ordered include Incoloy 800H, Inconel 617, Inconel X750 and Inconel 718. Bar and sheet will be ordered and multiple heats will be specified in order to check the consistency of mechanical behavior. At the present time there is some difficulty in locating more than one or two heats of the same material at a given supplier; therefore, several sources usually have to be contacted to obtain requirements.

5.1.1 Fatigue Testing of Incoloy 800H

A single test is currently running on a specimen of Incoloy 800H to compare with the old low-carbon (0.03%) heat which was used in all of the previous 1200 and 1400°F studies. The specimen is being tested at 1400°F at an alternating stress of $\pm$ 13.45 ksi. At the time of this writing, 1.6×10^8 cycles have been accumulated, which is approximately equal to the fatigue life of the old heat of Incoloy. A complicating factor in this test, however, is that the cycling has been interrupted several times because of power fluctuations.

5.2 Metal and Graphite Data Compilation and Review (P. Soo, J. Chow, S. Nicolosi)

The detailed review is continuing to establish materials data requirements for safety-related analytical studies on helium-cooled reactor systems. A limited amount of relevant work has already been compiled and analyzed in the "Nuclear Systems Materials Handbook" (TID-26666), including the physical and mechanical properties of Inconel 718, 2¼Cr-1Mo, and various austenitic stainless steels. Notable omissions, however, are Incoloy 800, Inconels 600 and 617, Hastelloy X and graphite.

In order to provide interim analytical data on these materials, available literature is being compiled and reviewed. Data of direct interest include physical, chemical, corrosion, and mechanical properties. The review of these data will establish where additional experimental information is needed and also will allow interim curves to be generated for design and analysis studies within Reactor Safety Research.

Current work has centered on the tabulation of pertinent physical and mechanical properties of Incoloy 800H, Hastelloy X, and various grades of graphite. It is planned to prepare a status report by the end of this year which will include all of the information tabulated to date.

5.3 Compilation and Assessment of Concrete (A. Auskern, L. Kukacka)

In the previous progress report it was pointed out that a large volume of the Fort St. Vrain PCRV is fabricated by the pre-

placed aggregate concrete (PAC) technique[5-1]. In this technique the coarse aggregate is first placed in areas of restricted access due to the congestion of reinforcing bars and/or tendon sheaths. The aggregate may be poured in or placed by shovel, but it must at some point be rodded to insure that it completely fills the available volume without bridging, that is, leaving large void volume within the concrete volume. A fluid grout is then pumped through a network of tubes into the preplaced aggregate and fills the interstices between the coarse aggregate pieces to form the preplaced aggregate concrete. The survey of the properties of preplaced aggregate that was begun in the preceding report period is continued here.

The application of PAC to massive construction is not new. The Corps of Engineers Waterways Experiment Station, for example, reports on a number of projects where PAC is used in parts of dams and powerhouses[5-2,5-3]. It has also been used in bridge piers, reactor shielding, and for dam repair work[5-4]. In general, concrete of adequate structural strength is produced by the prepacked technique. Extensive freeze-thaw testing of PAC and normal concretes show no difference between the two, so long as the PAC contains adequate air entrainment[5-3]. Extensive core testing from model PAC structures and testing of grouted cylinders showed that concretes of widely varying strengths can be produced[5-2]. Comparison between molded and grouted test cylinders of the same composition indicated that the molded cylinders (that is, conventionally mixed and placed) were 10-20%

stronger than the grouted test cylinders[5-2].

Some of the differences between preplaced aggregate and normal concrete placement techniques are summarized here:

(1) The preplaced aggregate is of a more uniform size range than normal aggregate.

(2) The preplaced aggregate must be free of dust and fines to insure a good grout-aggregate bond.

(3) The formwork must be stronger and more tightly constructed than formwork for normal concrete.

(4) Grout and vent tubes must be placed.

(5) Grout flow properties must be continuously monitored. Also, the progress of the grout during pumping must be followed, usually by using dip tubes which are kept in place.

(6) Facility must be made to prevent the grout from lifting the top few inches of aggregate.

(7) Techniques for testing for completeness of grout filling must be developed.

(8) Specialized equipment and well trained supervisory personnel must be used.

It is obvious that the use of preplaced aggregate concrete for massive structures represents a more involved and difficult type of construction.

The use of prestressed concrete as a reactor pressure vessel began in 1956[5-5]. Conventional concrete construction practices were used in these reactors. In the Wylfa pressure vessel, preplaced

aggregate was used in some congested areas near liner penetrations[5-5].

The Fort St. Vrain reactor represents the most extensive use to date of preplaced aggregate concrete. As indicated earlier this type of construction is used for the core support floor and the PCRV bottom head[5-6,5-7]. This represents a significant volume of the pressure vessel. There has not been an extensive amount of research work on PAC as applied to PCRV's, apparently for two reasons. It is assumed that PAC behaves the same as normal concrete[5-7], and secondly, PAC, until Fort St. Vrain, was not a major PCRV material[5-5]. The development work of PAC for the Fort St. Vrain PCRV was concerned with preparing a suitable high strength, low temperature rise (during hydration) grout-aggregate system. This objective was achieved and is documented in the report of Davis[5-8]. However, a number of important properties of the PAC, although considered, were not measured. These properties are shrinkage, creep at different temperatures, strength and modulus at elevated temperatures, and the effect of temperature cycling on PAC properties. It continues to be assumed that the PAC properties are similar to those of normal concrete of the same strength, and that the allowed design tolerances can cover real differences in behavior. A good example of this is Poisson's ratio. For PAC cylinders the average Poisson's ratio is 0.20. This value is larger than that obtained from the concrete properties test program (0.15 for Phase I and 0.13 for Phase II). For the PCRV stress analysis a value of 0.167 was used[5-6].

It would be anticipated from the macrostructure of PAC that properties like shrinkage and creep would be lower than for normally placed concrete. This is because of the point-to-point contact of the large aggregate in this material. Some limited work done on PAC used for radiation shielding (containing some iron shot aggregate) showed considerably less shrinkage than other normally placed shielding concretes, and temperature cycling to relatively high temperatures (~300°C) showed an expansion[5-9]. This might indicate a ratcheting effect resulting from thermal expansion differences between aggregate and grout coupled with the coarse aggregates being in contact.

In view of the recognized and potential differences between PAC and normal concrete and in the interest of completeness it would appear desirable that measurements be performed to obtain the lacking PAC data. Using the measured properties of the PAC material and their variations with temperature would permit a more complete stress analysis of the vessel to be performed.

5.4 Microstructure and Fracture of HTGR Graphites (J. E. Zimmer, R. A. Meyer, The Aerospace Corporation)

The approach for this program is to determine the relation of microstructure to the mechanical and fracture behavior of HTGR graphites and the effect of oxidation on these relationships. Crack propagation studies are being conducted on three HTGR graphites: Union Carbide ATJ graphite used for structural support posts, Union Carbide PGX graphite used for the support blocks, and Great Lakes Carbon H451 moderator graphite. A wedge-opening, crack-propagation

specimen is stressed and observed in the scanning electron microscope. This specimen is 2 mm thick with a half-thickness, V-shaped groove along the back to assure a relatively straight crack path. Controlled crack growth occurs with this specimen and direct observation of cracking and the graphite microstructure is made. Ion etching with xenon of the specimen surface delineates the individual microstructural features present, which provides identification of the microstructure at each point along the crack path. Oxidation studies are being conducted on the ATJ and PGX graphites to determine how oxidation affects the graphite microstructure and fracture behavior.

5.4.1 Crack Propagation

Crack propagation studies on the PGX graphite have assisted in identifying those microstrucural features that affect fracture of this graphite. A section of the crack path in the PGX graphite is shown in Figure 5-1. The crack, just left of center, tended to follow the pores that outline dense regions. This is evident in Figure 5-2 where the crack coincided with a line of pores (near the bottom) and also was diverted by the large grain in the center. The pore structure in PGX graphite seems to be a function of the incomplete packing of relatively large filler coke grains during fabrication. An example is shown in Figure 5-3. The fracturing in PGX graphite thus is controlled by these large pores that tend to be colinear.

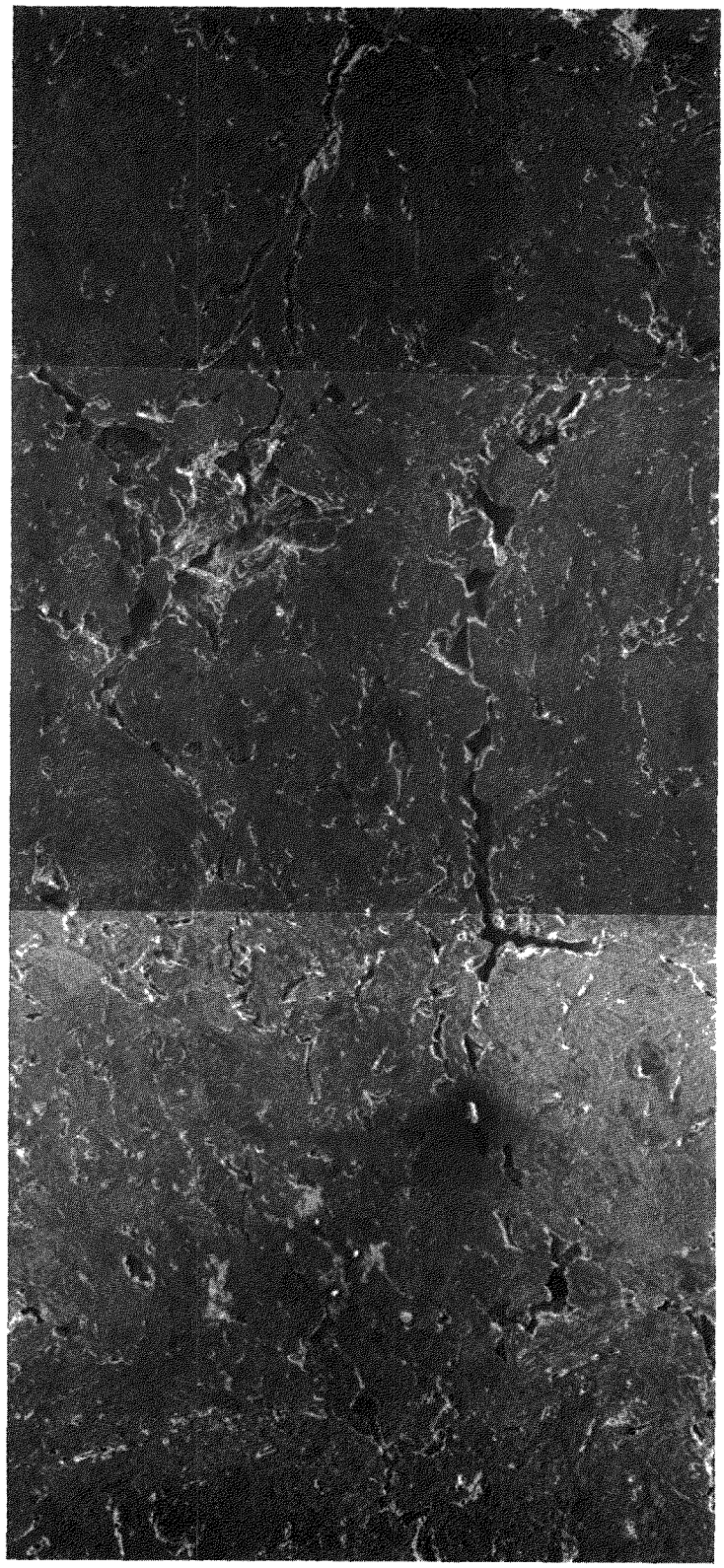

50X

Figure 5-1. Scanning electron micrograph of crack path in PGX graphite.

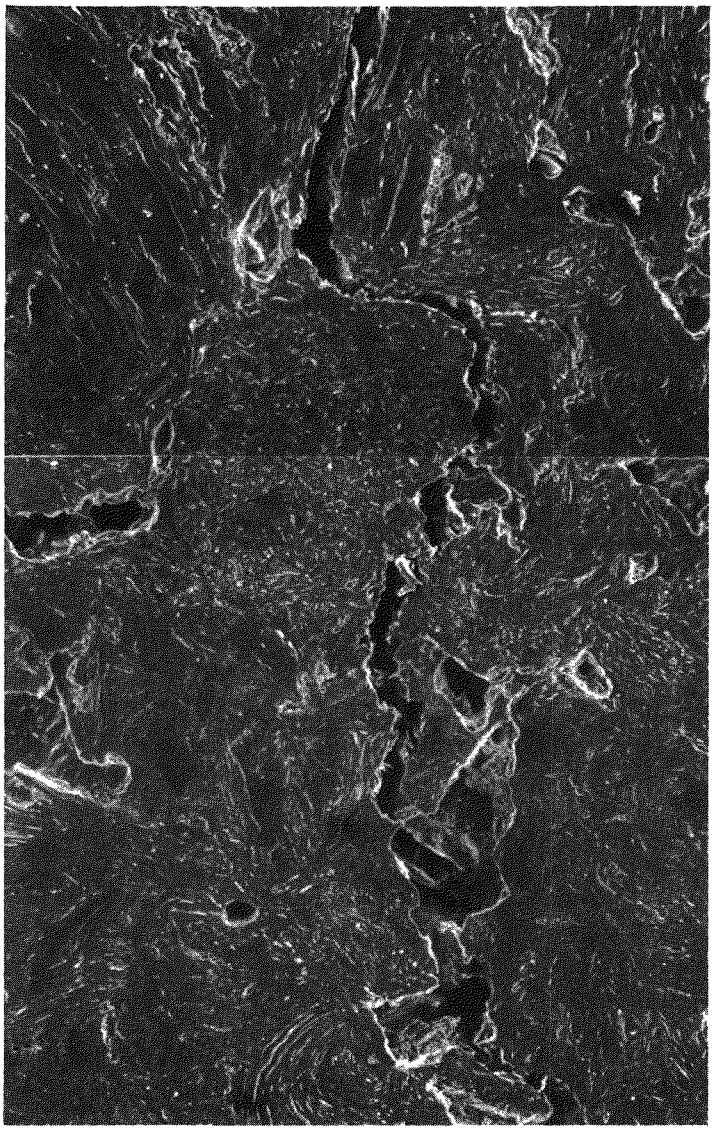

360X

Figure 5-2. Scanning electron micrograph of crack path in PGX graphite.

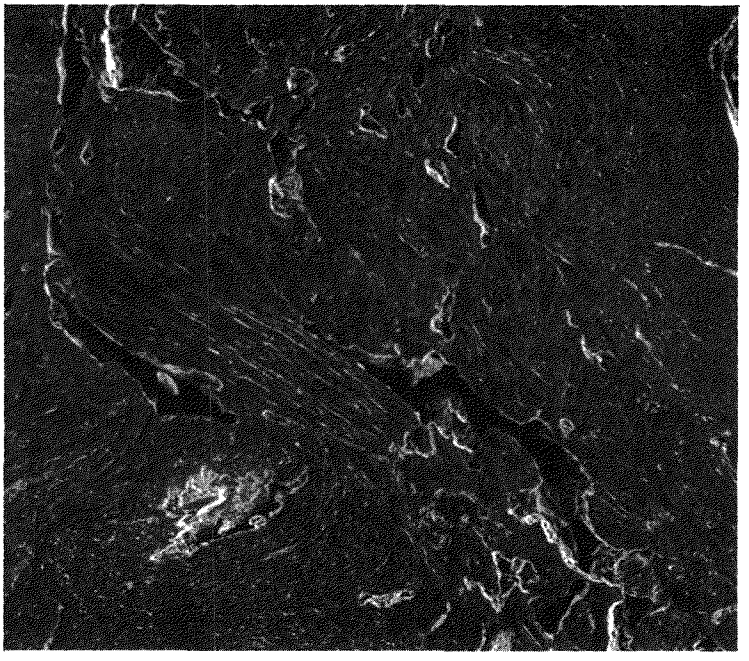

110X

Figure 5-3. Scanning electron micrograph of incomplete packing of large grains in PGX graphite.

5.4.2 Oxidation

To study the effect of oxidation on the microstructure, and subsequent fracture behavior, of HTGR graphites, specimens of ATJ and PGX graphite were oxidized in air for 1 hour at various temperatures. The attempt here was not to simulate the actual oxidizing atmosphere of the reactor but to obtain variations in weight loss and changes in the microstructure that might occur during the reactor lifetime. The specimens were inserted into a 1-inch diameter alumina tube furnace which was evacuated for about 15 hours. The specimens were heated to the specified temperature in a vacuum (< 40 microns) before being exposed to air. The air was desiccant dried and the flow restricted to 2 SCFH at 0.4 psig. The specimens were cooled in vacuo. Three types of specimens were used: 1/2-inch x 1/2-inch x 1/8-inch slabs for optical microscopy, 1/2-inch cube for study of the depth of oxidation, and 1/4-inch cubes for porosimetry measurements.

The weight losses as a function of temperature for the two graphites are given in Tables 5-1 and 5-2. The difference between the weight losses of the 3 types of specimens is probably due to the difference in the exposed surface area to volume ratio. At a given temperature, the ATJ graphite has about twice the weight loss of the PGX graphite. Also, the range of temperatures between 450°C and 550°C produce a large variation in weight loss. This variation should be helpful in observing the changes in the graphite microstructure as a result of oxidation.

Table 5-1

Oxidation of ATJ Graphite[1]

Specimen	Percent Weight Loss		
	450°C	500°C	550°C
1/2-inch slab	0.37	2.7	12.9
1/2-inch slab	0.46	0.36[2]	9.4
1/2-inch slab	0.23	1.1	10.4
1/2-inch cube	0.16	0.67	2.6
1/4-inch cube	0.51	1.7	14.2
1/4-inch cube	0.33	2.7	8.8
1/4-inch cube	0.66	2.8	12.8

(1) Specimens oxidized in dry air for 1 hour at 2 SCFH and 0.4 psig.

(2) No apparent reason for low value.

Table 5-2

Oxidation of PGX Graphite[1]

Specimen	Percent Weight Loss		
	450°C	500°C	550°C
1/2-inch slab	0.14	1.1	4.5
1/2-inch slab	0.13	1.2	4.9
1/2-inch slab	0.11	0.95	4.3
1/2-inch cube	0.08	0.41	2.1
1/4-inch cube	0.07	0.47	0.74
1/4-inch cube	0.84	0.75	3.1
1/4-inch cube	0.14	0.38	1.5

(1) Specimens oxidized in dry air for 1 hour at 2 SCFH and 0.4 psig.

The initial microscopy of the oxidized specimens has included low-magnification micrographs of a cross section through the 1/8-inch thick slabs. The micrograph for one ATJ specimen oxidized at 500°C is shown in Figure 5-4. The weight loss of 1.1% corresponds to about an increase of 8% porosity. A micrograph of unoxidized ATJ graphite is shown in Figure 5-5 for comparison. The oxidation appears uniform and is manifested by a slight increase in pore size. A similar set of micrographs for PGX graphite, oxidized at 500°C (Figures 5-6 and 5-7) shows that here the effect of the oxidation is not obvious. It should be noted that these are examples of the initial reference micrographs; higher magnification microscopy is needed to further clarify the effect of oxidation on these two graphites.

Detailed microscopy of the oxidized specimens of ATJ and PGX graphite will be continued. Porosimetry measurements will be made to quantitatively determine the change in pore size and distribution. The fracture behavior and the mechanical properties, as predicted by the analytical model, will be investigated as a function of the oxidation.

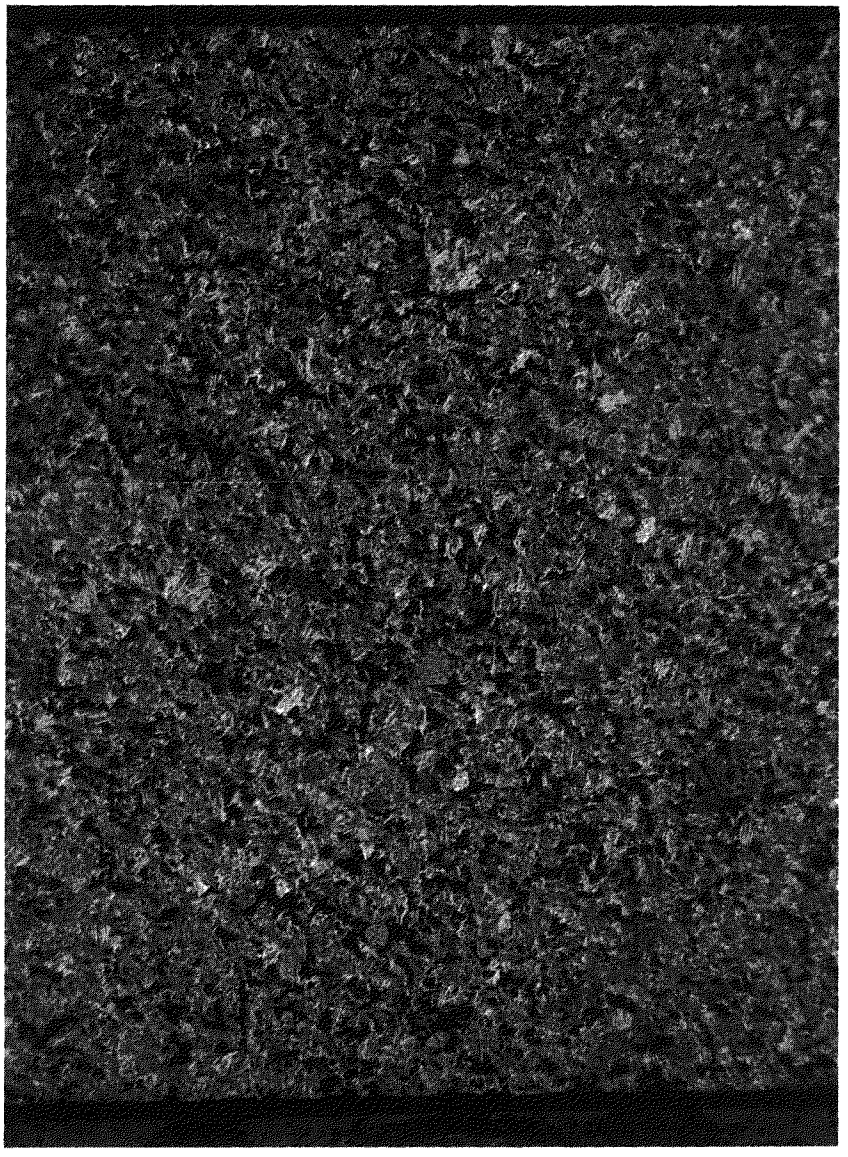

50X

Figure 5-4. Optical micrograph of through-thickness cross section of ATJ graphite oxidized in air at 500°C, 1.1% weight loss.

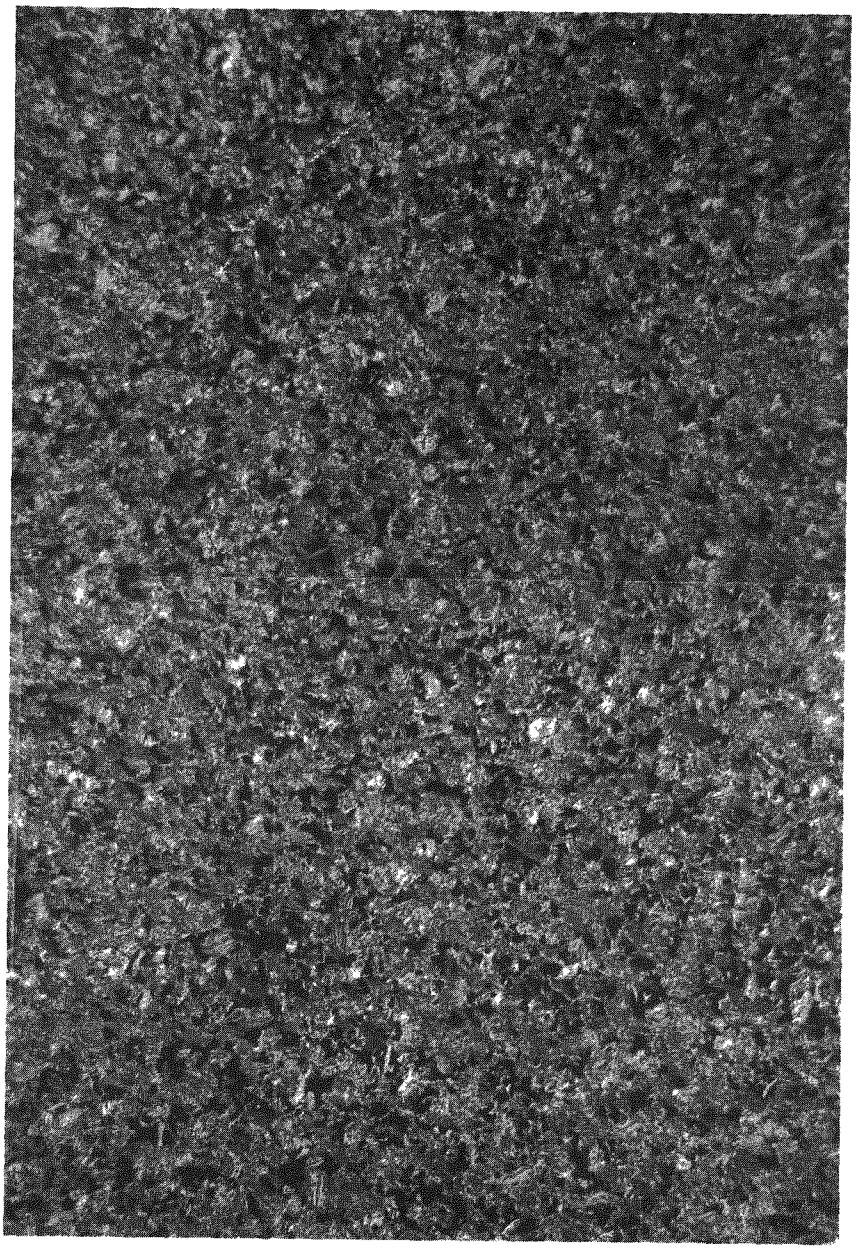

50X

Figure 5-5. Optical micrograph of unoxidized ATJ graphite.

50X

Figure 5-6. Optical micrograph of through-thickness cross section of PGX graphite oxidized in air at 500°C, 1.1% weight loss.

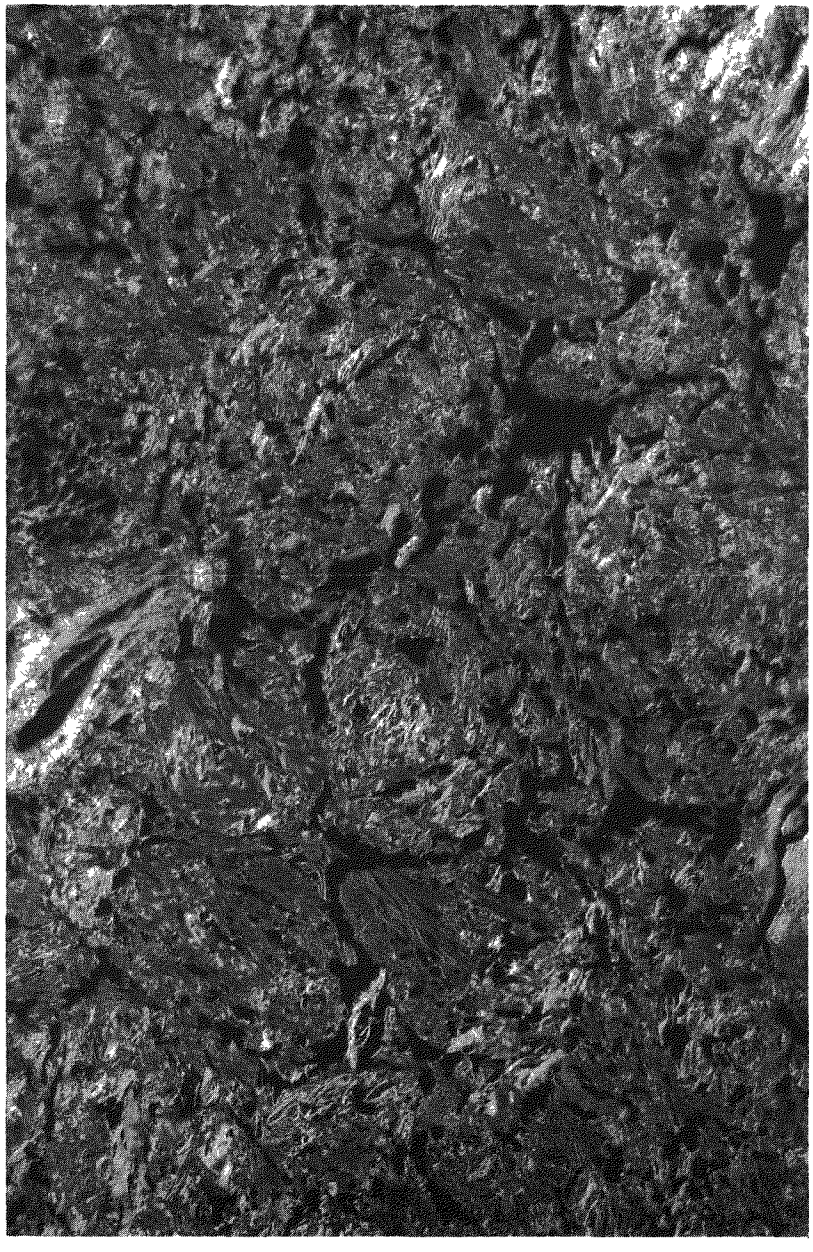

50X

Figure 5-7. Optical micrograph of unoxidized PGX graphite.

References

5-1 HTGR Safety Evaluation Division Quarterly Progress Report, July-September 1975, BNL-50479.

5-2 Investigation of the Suitability of Prepakt Concrete for Mass and Reinforced Concrete Structures, TM 6-330, Waterways Experiment Station, Vicksburg, Miss., October 1951.

5-3 Ibid: Appendix A and B, August 1954.

5-4 Preplaced Aggregate for Structural and Mass Concrete, American Concrete Institute Journal, October 1969, pp. 785-97.

5-5 Chen Pang Tan, "Prestressed Concrete in Nuclear Pressure Vessels: A Critical Review of Current Literature." ORNL-4227, May 1968.

5-6 Final Safety Analysis Report, Fort St. Vrain Nuclear Generating Station, Vol. II, Section 5.4.

5-7 Prestressed Concrete Reactor Vessel Model 2, CTA-715D, General Atomic Division, General Dynamics Corporation, San Diego, Calif., 1966.

5-8 Raymond E. Davis, "PAC Test Program Phase B." Report to the Prepakt Concrete Company, Cleveland, Ohio and Gulf General Atomic, San Diego, California, May 1968.

5-9 H. S. Davis, "N-Reactor Shielding," paper SP34-52 in Concrete for Nuclear Reactors, Vol. II, pp. 1109-61, American Concrete Institute, Detroit, 1972.

6. Task Area VI - Safety Instrumentation and Control System

6.1 Monitoring for Impurities in the Primary Coolant at Fort St. Vrain (L. Green)

The purpose of this program is to measure the impurities in the primary coolant over a wide range of actual plant operating conditions. The data will be obtained using a mass spectrometer (MS) so that comparisons can be made with the plant's data and data from other experimental monitoring programs. (The LASL experiments with the "He-Afterglow" device for example.)

A MS was selected because it has a capability for measuring a wide range of impurities at very low levels of concentration. The MS will also provide a method of measurement that is unique from the method used by the facility or from methods proposed in other experiments. Specifications for the MS require that it be capable of identifying and measuring Xe, Kr, Ar, Cs and I at concentrations of 1 ppbv; and H_2, tritium, CH_4, O_2, H_2O, CO, CO_2 and N_2 at 1 ppmv. In the low mass range, 1-40 AMU, a fairly high resolution will be required to resolve CO (MW 27.9949) and N_2 (MW 28.0061).

Fort St. Vrain has been selected because it will be the only commercial HTGR in operation over the next few years. During visits to the Fort St. Vrain facility the possible location of the MS was discussed with some of the Fort St. Vrain staff. Three possible locations have been identified and are proposed to the Fort St. Vrain management. The three locations are:

1. The Pipe Gallery Area - surrounds the PCRV and has a number of walkways constructed of steel grating that are adjacent to the moisture and process instrument penetrations. Two "Fast Gas Sampling Manifolds," one for each loop, are located in this area. The length of the sample line to each manifold is about 20 feet. These manifolds are possible points for connecting the instrument. Connections at any of 8 instrument penetrations may be possible. Disadvantages are high ambient temperature and humidity, and limited floor space. Locating the MS in the Pipe Gallery is the preferred arrangement, since the sample line would be the shortest. A solution to the temperature and humidity problem would be to separate the two components of the MS, the Analyzer System from the Electronics Cabinet. The Electronics Cabinet could be located in an air conditioned area, such as the Analytical Instrument Room, and the Analyzer System, which is not affected by high temperature and humidity could be located in the Pipe Gallery Area. About 6 small electrical cables would be needed to connect the two components of the MS.

2. The Analytical Instrument Room - contains the instruments for monitoring coolant impurities. Impurities are measured with a gas chromatograph and an infrared analyzer. Gas samples are piped directly to the instrument panel in the room. The sample line is 1/16-inch I.D. stainless steel tubing about 300 feet long. Gas pressure is about 15 psig. The LASL "He-Afterglow" device was

operated in this room and will probably be used again after start-up. The room is air conditioned which provides a good environment for the MS. Connecting to the sample line would be relatively simple, but length of the sample line would be a disadvantage. Limited floor space may also be a problem if both components of the MS were located here.

3. The Turbine Floor - this area was not discussed as a possible location for the MS but is mentioned because other instruments are located there. The environment and floor space would be ideal for the Electronics Cabinet but the area is fairly remote from the reactor. A sample line to the Analyzer System about 1000 feet long might be required; too long to be practical for this experiment.

MS measurements are expected to continue for a period of 6 months to a year so that the data collected will span a wide range of plant operating experience. Although it is expected that the MS will be unattended during evenings and weekends, daily checks on the instrument's operation will be required. These checks will require that one individual be assigned to monitor the instrument and perhaps correlate the MS data with plant operating data.

6.2 Other Monitoring Techniques (L. Green, H. Isaacs)

Following the initial MS experiments at Fort St. Vrain the testing of an Electrolytic Oxygen Activity Meter, discussed in section 2.2, has been proposed. This instrument could be used to

monitor changes in oxygen activity of the helium coolant. Since such changes are influenced by impurity levels, the instrument could serve as an impurities monitor. Tests have shown that the instrument is sensitive to free oxygen levels to less than 1 ppmv and has a rapid response to the changes in impurity levels in the He gas.

7. Task Area IX - Phenomena Modeling and Systems Analysis

7.1 HTGR Safety Code Library (J. Beerman, J. Colman)

The General Atomic (GA) developed UNIVAC computer code SORSG-GASSAR/6-75 was acquired from GA and conversion initiated. Work has stopped pending receipt from GA of sample test input and output.

The GA codes CORCON-GA-LTR-13, SORSD-GASSAR/6-75 and TAP have been converted and are now operational on the BNL CDC-7600 computer system.

Table 7-1 summarizes the status of the 31 programs now being maintained in the Library.

7.2 GOPTWO Computer Program (L. Epel)

The previous quarterly progress report presented the results of sensitivity analysis on HTGR's obtained with the GOPTWO code. Those computations presented the effect on helium impurities of varying the graphite-water reaction rate, the diffusion coefficient of water vapor in graphite and the water ingress rate. Among the inherent assumptions in the calculations was the value of the mass transfer coefficient between helium and the surface of the graphite; it was taken to be infinite. This is necessitated by the GOPTWO program itself, which has built into its coding the assumption that the water vapor concentration at the graphite surface (of a cooling channel) is the same as in the helium free stream. Some questions concerning the validity and effect of this assumption concerning the mass transfer coefficient were raised during presentation of the re-

Table 7-1

HTGR Safety Code Library

Program	Status	Proprietary	Function
CRECT	OP	NP	Corrects data on ENDF/B tape.
LISTFC	OP	NP	Lists data from ENDF/B tape.
RIGEL	OP	NP	Manipulates data on ENDF/B tape.
ENDFB2	OP	NP	Converts data on ENDF/B tape to binary.
FLANGE	OP	NP	Prepares thermal cross section transfer arrays.
GAND2	OP	NP	Prepares fine group fast, resonance, and thermal cross sections from ENDFB2 binary tapes.
GFE2	OP	NP	Prepares fine group fast cross sections from ENDFB2 binary tapes.
MAKE	OP	NP	Prepares fine group fast cross section tape from GFE2 for spectrum codes.
WTFG	OP	NP	Prepares fine group thermal cross section tape from GAND2 or FLANGE for spectrum codes.
PRINT	OP	NP	Reads the fast cross section tape produced by MAKE.
SPRINT	OP	NP	Reads the thermal cross section tape produced by WTFG.
GGC4	OP	NP	Prepares broad group cross sections from MAKE and WTFG tapes.

C = In the process of being converted to the CDC-7600.
OP = Operational on the BNL CDC-7600 system under Scope 2.
R = Recently received from General Atomic Co. or Argonne Code Center.
P = General Atomic Company proprietary code.
NP = Not considered to be a proprietary code.

Table 7-1 Cont'd.

Program	Status	Proprietary	Function
INTERP	OP	NP	Prepares broad group cross sections from MICROX output data tapes.
1-DX	OP	NP	Performs one-dimensional, diffusion theory, steady-state calculations.
FEVER-7	OP	NP	Performs one-dimensional, diffusion theory, burnup and reload calculations.
TEMCO-7	OP	NP	Computes reactor temperature coefficients from input cross section data.
BLOOST-7	OP	NP	Performs zero-dimensional reactor kinetics calculations.
GAKIT	OP	NP	Performs one-dimensional reactor kinetics calculations.
TWIGL	OP	NP	Performs two-dimensional light-water reactor kinetics calculations.
TAC-2D	OP	NP	Performs two-dimensional, transient conduction analyses.
FLAC	OP	NP	Calculates steady-state flow distributions in arbitrary networks with heat addition.
POKE	OP	P	Calculates steady-state flow distribution and fuel and coolant temperatures in a gas-cooled reactor.
RECA	C	P	Calculates time-dependent flow distribution and fuel and coolant temperatures in the primary system.
CORCON	OP	P	Computes the temperature history and fission product redistribution following a loss of all convective cooling of the core.
SORSD	OP	P	Computes the release of volatile fission products from an HTGR core during thermal transients.

Table 7-1 Cont'd.

Program	Status	Proprietary	Function
GOPTWO	OP	NP	Analyzes the steady-state graphite burnoff and the primary circuit levels of impurities.
OXIDE-3	OP	P	Analyzes the transient response of the HTGR fuel and moderator to an oxidizing environment.
SAMPLE	OP	NP	Propagates uncertainties in probability distributions by Monte Carlo technique.
TAP	OP	P	Calculates the transient behavior of the integrated HTGR power plant.
SORSG	C	P	Computes the release of non-volatile gaseous fission products from an HTGR core during thermal transients.
DIFFTA	OP	NP	Solves the steady-state, two-dimensional diffusion equation by finite element method.

sults to the Division of Technical Review. Therefore, the GOPTWO code was modified to allow for the specification of any mass transfer coefficient and subsequently a series of cases were run to study the impact of varying this parameter.

To implement this change in the GOPTWO program it was only necessary to reduce the graphite-water reaction rate appropriately to reflect the lower concentration of water which would result from a finite mass transfer coefficient, leaving the other reaction rates (i.e., $C + CO_2$, $CO + H_2O$, and $CO_2 + H_2$) intact. It is easy to show[7-1] that the water concentration throughout the graphite is reduced by a constant factor when the mass transfer coefficient is reduced from infinite to say, a value β. This constant, F, is simply:

$$F = \frac{\beta \varkappa_2}{\beta \varkappa_2 - \sqrt{Dk}\, \varkappa_3}$$

where D is the diffusion coefficient of steam in graphite, k is the volumetric reaction rate constant for steam in graphite, $\varkappa_1$, $\varkappa_2$, $\varkappa_3$ are dimensionless groupings of the modified Bessel functions of the first and second kind, of zero and first order. The arguments of the Bessel functions involve D, k and the diameter of the cylindrical coolant channel that GOPTWO considers. Specifically,

$$\varkappa_1 = I_1 \left(\frac{r_o}{L}\right) / K_1 \left(\frac{r_o}{L}\right)$$

$$\varkappa_2 = I_0 \left(\frac{r_i}{L}\right) + \varkappa_1 K_0 \left(\frac{r_i}{L}\right)$$

$$\varkappa_3 = I_1 \left(\frac{r_i}{L}\right) - \varkappa_1 K_1 \left(\frac{r_i}{L}\right)$$

where r_i is the inside radius of the coolant channel, r_o is the equivalent outside radius of the coolant channel, L is $\sqrt{D/k}$.

These relations were programmed into GOPTWO and a series of cases were then run to see the effect of varying the mass transfer coefficient, all other variables being kept at their "nominal" values. The results are shown in Figure 7-1. It can be seen from this figure that, for nominal operating conditions in the HTGR, any mass transfer coefficient greater than about 1 cm/sec gives essentially the same results as when the mass transfer coefficient is infinite.

To judge the validity of the original GOPTWO assumptions concerning the mass transfer coefficient an estimate of the mass transfer coefficient during nominal flow, power, temperature, pressure, etc. conditions in an HTGR was made. A typical value is in the neighborhood of 10 cm/sec which, according to Figure 7-1, gives results equivalent to those attained assuming that the mass transfer coefficient is infinite. Thus, at full flow conditions (and well below full flow as well) the inherent assumption programmed into GOPTWO is quite valid.

7.3 Finite Element Method Diffusion Program (L. Epel)

A two-dimensional, steady-state diffusion code that utilizes the finite element method has been written[7-2]. This code solves problems such as:

(1) Heat conduction in x-y and r-z geometry and includes the effects of thermal radiation between elements, temperature-dependent

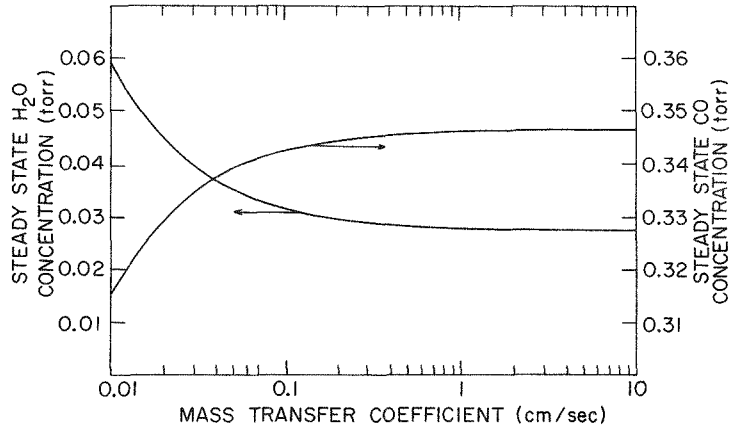

Figure 7-1. Effect of mass transfer coefficient on GOPTWO results for nominal HTGR case.

conductivity, and anisotropic conductivity. Heat sources and/or sinks can be included in the analyses.

(2) Neutron diffusion in x-y geometry. The diffusion coefficient can be anisotropic and it, as well as the absorption cross-section, can be flux-dependent. This dependence is of the form: $D = D_0 + D_1\varphi + D_2\varphi^2$.

(3) Fission product migration problems. These, being completely analogous to heat conduction problems, can be done in x-y or r-z geometry, can have diffusion coefficients that are dependent on concentration, and can account for anisotropy of the diffusion coefficient. Sinks and sources are, of course, possible, but there is no analog to thermal radiation in such problems.

The user has the option of using the Gauss-Seidel method of solving the matrix generated during the solution, or alternatively solving directly by inversion. At present, the number of elements and nodes is limited to a maximum of 100 and the number of boundary nodes and surfaces contributing to radiative heat transfer is limited to a maximum of 25. These limitations can easily be removed by simply changing some dimension statements in the FORTRAN.

The only boundary conditions possible with the code in the present form are those in which the dependent variable (i.e., the temperature, neutron flux, nuclide concentration, etc.) is either zero at the boundary or has a zero normal derivative there. Convective boundary conditions can be simulated by the simple artifice of specifying a layer of fictitious material, having a thermal conduc-

tivity and thickness that together yield a resistance equivalent to the film resistance.

Some thought is being given to the possibility of expanding the code's capabilities in order to allow it to solve time-dependent problems.

7.4 Systems Code Development (L. Epel)

Work performed with TFR to date has resulted in an auxiliary computer program which has been named SYMSIM, an acronym for System Simulation. It is an outgrowth for the need to test separately, individual component models for TFR. The program is basically a non-linear ordinary differential equation solver routine with various sub-routines that calculate derivatives. It has grown into a model in its own right and at present it can be used to study systems for which the working fluid is a perfect gas. A short description of the code and a sample calculation are presented below:

The basis of SYMSIM is a routine that solves systems of non-linear, first order, ordinary differential equations. Because of availability and simplicity in implementing the routine, the Runga-Kutta-Merson technique with automatic time-step size adjustment as outlined and programmed in Reference 7-3 is currently used. Other programmed integration schemes could have been used, such as GEAR[7-4] or Hammings Predictor-Corrector Method[7-5] and indeed may be included as an option in the future. Data for a problem is read by the program and initial conditions are calculated. The differential equation solver then takes over by calling a sub-routine that calculates all

derivatives. This routine in turn calls routines that calculate specific derivatives. The differential equations that are solved are the conservation (mass, momentum, energy) equations, the neutron kinetics equations, and those describing heat transfer in the reactor core and in heat exchangers. After the equations are numerically integrated the desired results are printed as a time history, showing flows, temperatures, energy contents, pressures, etc. as desired by the user.

The sample calculation was done to compare the results of SYMSIM to those obtained from TFR. The problem is a simple one involving two volumes (20 ft^3 each) connected by a junction whose frictional resistance and inertance are specified. Both volumes are filled with helium, assumed to behave as a perfect gas, at $1416^{o}F$. Volume 1 is pressurized to 710 psia and Volume 2 is at 500 psia initially; then flow is allowed to commence between the two volumes. The entire system is assumed to be adiabatic. It was found that the results of SYMSIM agreed with those of TFR within 1/2% over the entire history of the transient.

An interesting consequence of the calculations is the oscillatory behavior of the junction flow. In Figure 7-2 the flow from Volume 1 to Volume 2 is shown for the first 12 milliseconds (the problem was carried out to 100 milliseconds but the characteristics of the flow did not change from those depicted). The conditions of the problem for cases A, B, and C were the same except for the value of the friction factor in the momentum equation; this was $f\frac{L}{D} = 0.1$,

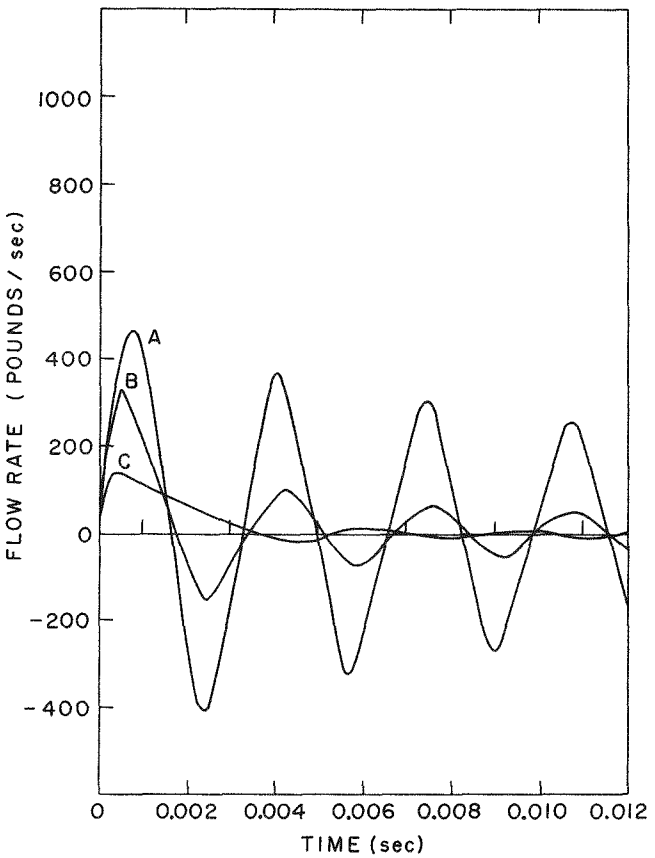

Figure 7-2. Junction flow for test problem.

1.0, and 10, respectively. As expected, an increase in the friction factor results in a dampening of the oscillations. Interestingly, an increase in friction factor also affects the shape of the waves, skewing them and bringing them out of phase with one another. Although it was not done in time to include in this quarterly report, a critical value of friction factor can probably be found that dampens the system enough to just avoid reverse flow between Volume 1 and Volume 2 and thus eliminate any oscillation. Beyond that critical value the unidirectional nature of the flow would be unchanged but the time for complete discharge of the gas from one volume to the other would continually increase as the friction factor increased. This would be accompanied by a decrease in the peak value of junction flow.

7.5 OXIDE-3 (J. Skalyo, Jr.)

The GA code OXIDE-3[7-6] has previously been utilized for the calculation of equilibrium impurity concentrations in the primary coolant stream resulting from different constant steam leak rates while operating at full power[7-7,7-8]. Parameter sensitivity studies were also done on what were thought to be the most relevant parameters:

(1) The steam-graphite reaction rate.

(2) The steam mass-diffusion rate in graphite.

These calculations were compared with results obtained from the GOPTWO code and also served to aid in scoping the physical regimes of interest in an experimental graphite oxidation program. The accuracy one obtains in analyzing the transient response of an HTGR following accidental inleakage of steam and/or air into the primary coolant

system is dependent upon both the data base used in the code and the sufficiency of the HTGR model implemented in the code.

However, additionally there are many mathematical methods[7-9] which could be used to solve the HTGR model equations, and in the present quarterly report attention is focused on the adequacy of the OXIDE-3 solution. In particular, the reactor core is divided into 20 refueling regions with the intra-region columns of fuel blocks being similar; the vertical columns are further divided into 10 layers with varying power factors determined by designed fuel loading. The results obtained in an OXIDE-3 calculation are then directly dependent upon the finite difference method solution of the heat/mass transfer which occurs in the OXIDE-3 symmetry element (the result is the same for all elements in the same layer and the same region). The OXIDE-3 symmetry element and its important dimensions are shown in Figure 7-3. The completely implicit solution to the resulting finite difference equations for each of 200 symmetry elements is obtained by the efficient solution of a matrix equation of minimum bandwidth 5 (the numbering of connecting nodes and its relation to minimize the matrix bandwidth is also a well known problem in finite-element techniques; the one dimensional problem would give a tri-diagonal matrix equation).

The effectiveness of the implicit finite difference solution and of the mesh size has been questioned in a first round DOL review of OXIDE-3 (in particular, questions 2a and 2b):

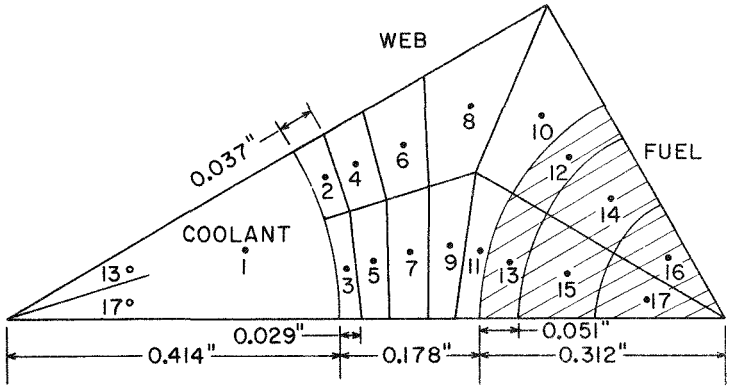

Figure 7-3. Oxide 3 symmetry element.

"Q.2a & Q.2b (AEC Letter 6/21/74) QUESTION:

(a) Describe any comparisons made with OXIDE-3 of analytical solutions of diffusion processes, either of mass or heat diffusion. Provide, if possible, an OXIDE-3 solution to Case XV on Page 233 Carslaw and Jaegar.

(b) Discuss the noding sensitivity in OXIDE-3. What improvement would be gained by using a finer noding scheme? Please vary the number of placements of the node areas in the sample problem (Chapter 9) to demonstrate the insensitivity of the results to mesh size. Include a more detailed sample editing such that linear heat and material fluxes between nodes are available."

Question 2a is answered in Amendment 1 to GA-LTR-7 (OXIDE-3); as expected, the long experience of success achieved over many years with the implicit finite difference solution of the diffusion equation is demonstrated on a textbook problem. However, the important Question 2b is not answered; the use of the OXIDE-3 algorithm to solve a textbook problem ignores the question. In the following discussion, an attempt is made to shed some light on the specifics of Question 2b.

The approach here is to justify a particular mesh spacing a priori by simplification of the OXIDE-3 symmetry element based on physical principles and additionally to then refine the OXIDE-3 element based on these results. The basic premise to be followed is that a mesh for an OXIDE-3 calculation should be at least as good as that which would be necessary to solve the steady-state one dimensional diffusion equation with space-independent coefficients. Additionally,

the mass transfer problem with its non-linear temperature dependent coefficients appears to offer more severe program limitations arising from the use of a fixed mesh than the heat transfer problem. One might also presume that most of the adverse steam- and/or air-graphite reactions will take place at the higher temperatures and therefore predominantly at the surface of the coolant channel; thereby giving justification to the valid reduction of the problem to one dimension.

The equivalent OXIDE-3 one dimensional steady-state diffusion reaction differential equation is:

$$Z \frac{\partial^2 C}{\partial X^2} - KC = 0$$

where C is the concentration, Z is the effective diffusivity, and K is the reaction rate constant. The solution in a semi-infinite solid is:

$$C = C_o \exp\left(-\sqrt{\frac{K}{Z}}\, X\right).$$

An adequate finite difference solution to the problem might be jeopardized when the mesh spacing is larger than $L = \sqrt{\frac{Z}{K}}$. Utilizing equations for K and Z given in OXIDE-3, values for L were calculated as a function of temperature and are shown in Figures 7-4 to 7-6 for the graphite-steam, graphite-oxygen and fuel rod-steam reactions, respectively.

The relevant mesh spacings to be compared are indicated on the figures; these are the distance from the coolant channel surface to either mesh point 2 or mesh point 3 for the first two reactions and the distance from the fuel rod-web gap to mesh point 12 or mesh

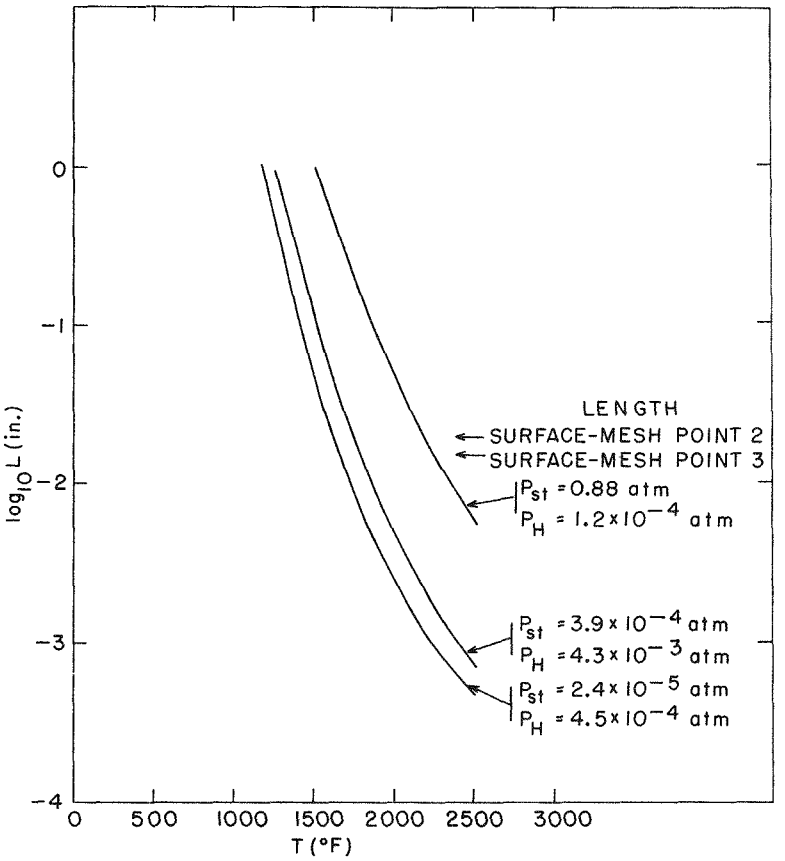

Figure 7-4. Graphite - steam, reactant length vs. temperature.

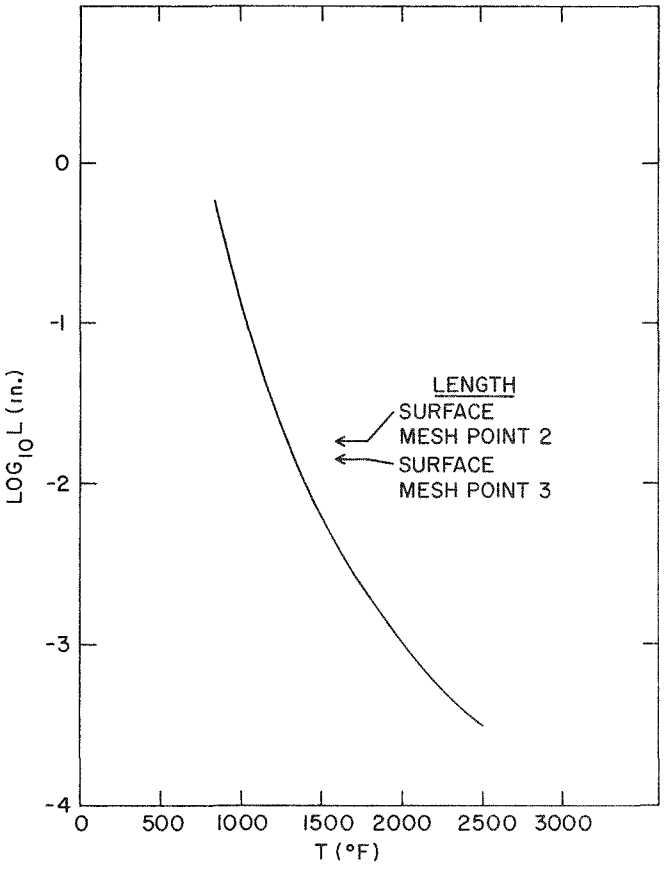

Figure 7-5. Graphite - oxygen, reactant length vs. temperature.

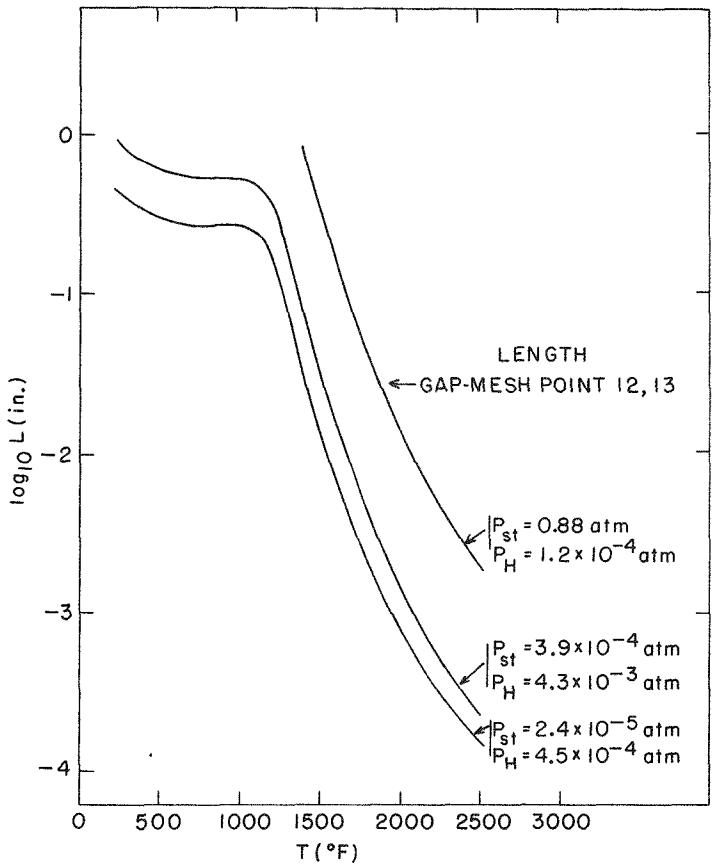

Figure 7-6. Fuel rod - steam, reactant length vs. temperature.

point 13 for the last reaction. The fuel rod-steam reaction rate constant consisted of both a graphite-steam reaction that was taken as ten times that of the graphite web-steam reaction constant and a fuel hydrolysis reaction which was calculated assuming a 1.6% fuel failure. Figures 7-4 and 7-6 show three different concentrations of hydrogen and steam which affect the Langmuir-Hinshelwood equation for the graphite-steam reaction. The top curve in each is the peak steam concentration that occurs in the steam inleakage problem illustrated in Chapter 9 of GA-LTR-7. This occurs approximately 24 seconds into the transient while the core is still quite hot. The lowest two curves are for equilibrium impurity concentrations in the primary coolant stream for constant steam leaks of 0.9 lb/h and 0.09 lb/h (upper and lower of the two curves, respectively).

It is apparent that any given mesh may give inaccurate answers if the temperature is high enough. The mesh spacing in the fuel rod is judged more than adequate. The knee in the curve of Figure 7-6 which occurs near 1200°F is the boundary wherein fuel hydrolysis dominates at low temperatures and the graphite-steam reaction dominates at high temperatures. After a scram following an accident, fuel hydrolysis will continue to take place when the temperature falls below ≈1000°F. The high temperature part of the curves in Figure 7-6 are only slightly shifted from the curves of Figure 7-4. The temperature at which the mesh spacing would be inadequate in the fuel rod occurs when the web graphite near the coolant channel surface is gettering most of the steam; hence, relatively little steam reaches

the fuel rod and the attendant error due to mesh size is of no consequence. At the low temperatures where the fuel hydrolysis dominates and the web graphite offers no protection, the mesh size in the fuel rod is more than adequate.

The temperatures where L for the web graphite is equal to the surface mesh point 3 distance, are 2250°F for the steam in-leakage transient problem of GA-LTR-7 and 1800 and 1660°F for the 0.9 lb/h and 0.09 lb/h steady-state steam leak, respectively. The mesh spacing should be adequate for the transient study whereas the steady-state calculation would have L values in a few of the hottest elements smaller than the mesh spacing.

The graphite-oxygen reaction, as with the steam-graphite reaction, occurs with significance only near the coolant channel surface. The temperature where L is equal to the surface to mesh point 3 distance, is shown in Figure 7-5 to be 1320°F. This would encompass a rather large portion of the lower layers of the core. It would seem that the appropriateness of the OXIDE-3 mesh spacing is inadequate for accurate air ingress calculations. It is noted that the curve in Figure 7-5 is quite steep and gives an L of 0.002 inch at only 1800°F.

Future advances in fuel particle development will allow the core to run at hotter temperatures, especially in a process heat HTGR. The increase in core temperatures will then necessitate changes in the OXIDE-3 mesh in order to assure the precision of its predictive capabilities. It is also desirable to have knowledge of the errors

encountered in the air ingress accident in the HTGR. Program alterations have, therefore, been initiated on OXIDE-3 which are necessary to implement changes in the mesh arrangement. The program as presently written utilizes almost all of the allocable direct access computational memory of the CDC 7600; it is therefore unfruitful to extend the nodal network beyond the present 3400 points (17 mesh points in each of 10 layers in 20 regions). An alternative approach has been decided upon by which the 17 nodal points are not changed; the geometric arrangement of the points has been altered in a manner thought to be more appropriate to the problem of mass transfer in the triangular symmetry element.

An initial scheme is shown in Figure 7-7. Heat transfer calculations[7-10] and indeed calculations of OXIDE-3 itself indicate that an extremely small θ-dependence is expected near the surface of the coolant channel. As a next step, another three nodes will be placed near the surface thus reducing the surface to mesh node 2 spacing to less than the indicated 0.0075 inch. These will be taken from the fuel rod area where again the θ-dependence is negligible.

The fuel rod-graphite web gap is taken into account in the heat transfer calculation in OXIDE-3 but neglected in the mass transfer. However, the existence of the gap would enhance the θ-independence of the concentration in the fuel rod (diffusion in the gap is 100 times that in the graphite). The various program changes necessary to reduce the fuel rod to less than the presently allotted 6 mesh points are being delimited.

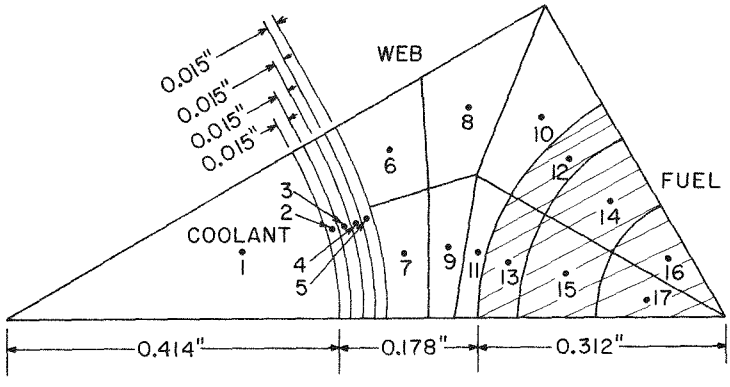

Figure 7-7. Revised oxide 3 symmetry element.

Along with the aforesaid mesh change, it has also been decided to compare the fully implicit calculation with that of a Crank-Nicolson scheme. Stability of the solution is not sacrificed, some improvement in accuracy is expected, and no sacrifice in maximum allowable time step is foreseen (the time step limit is set by other factors in the OXIDE-3 calculation).

7.6 SORS (J. M. Dickey)

The SORS codes compute the maximum hypothetical fission product release for a transient temperature sequence. New versions of SORSD and SORSG, which deal with the non-volatile and volatile fission products respectively, have been received from GA and converted to the CDC 7600. A complete set of input data and sample output are needed to test the new codes and have been requested from GA. The new versions of SORSD and SORSG differ from the earlier version of SORS described in LTR-10[7-11], in the methods used to calculate the fraction of fuel particles which has failed and the release rate from the fuel particles. The range of temperatures over which the coatings of the fuel particles fail depends on the irradiation time. In the new versions, the fraction of the fuel which is 1, 2, 3 or 4 years old is input and the number of failed coatings is calculated using the appropriate data for each age group; whereas previously an averaged failure rate was used. However, as mentioned before[7-8], the details of the failure of the fuel particle coatings are unimportant in determining the release of the fission products since failure occurs at relatively low temperatures, and even assuming complete failure of the coatings at the start of the accident results in an insignificant change in the

fission product release[7-8]. A more important parameter is the instantaneous rate at which the fission products escape from the fuel particles and the new method of calculating an average instantaneous escape rate for the whole reactor yields results different from the earlier version of SORS. Assuming the whole reactor to be at a uniform average temperature the release of the fission products appears to be delayed some 2 hours, but a complete discussion is deferred pending arrival of the requisite input data from GA.

The calculations in SORS are split into two parts. In the first part, the sub-routine FKCALC, the instantaneous escape rate of each element from the fuel particles at the local temperature is found and averaged over the whole reactor. These average fractional escape rates are used as time dependent coefficients in the differential equations for each decay chain which are then solved in the second part using an accurate numerical technique. FKCALC also calculates the activity released just using simple stepwise integration of the differential equation, neglecting decay, and, in many cases, gives a very close approximation to the results using the more sophisticated complete code. In Figure 7-8 is shown the amount of ^{131}I released calculated using SORS and the approximation using just the sub-routine FKCALC. The detailed thermal history of the core is important in determining the release. For comparison Figure 7-8 also shows the release of ^{131}I calculated using SORS assuming that at each instant the whole core is at a temperature equal to the

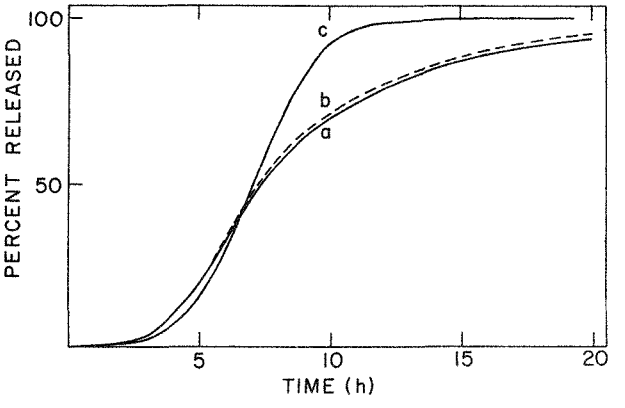

Figure 7-8. Release rate of ^{131}I (a) from SORS (b) from sub-routine FKCALC, both (a) and (b) are calculated using a thermal history of the reactor derived from CORCON, (c) from SORS with the whole core at the same temperature at each instant equal to the average temperature for case (a).

average temperature of the core. Initially the existence of local hot spots in the core results in a higher rate of release than for a core at a uniform temperature but at later times some of the fission products are retained in the cooler portions of the core. For a realistic prediction of the fission product release both a reliable temperature history of the core and experimental data on escape rates of the fission products from the fuel particles, are needed. It is not necessary to use a sophisticated numerical technique to solve the differential equations.

7.7 Reactor Physics - Generation of Two-Group Diffusion Parameters for the HTR Control Rod Assembly (J. W. Herczeg, C. Sastre)

7.7.1 Approach and Choice of Computational Method

The calculational approach necessary to generate standard diffusion theory parameters ("Group-Constants") for an HTR control rod fuel assembly differs significantly from the standard "unit cell" approach commonly employed on a fuel stick surrounded by a moderator. Several computer codes are available which can handle specific problems such as extreme variation in neutron current, complex geometries, effective void regions and the like. Such problems can be treated by Discrete Ordinate (S_N) Theory (DS_N). Several DS_N codes are available; a few are DTF-IV[7-12], ANISN[7-13], TWOTRAN-II[7-14] and TRIPLET[7-15]. The selection of the code is mainly dependent on the users geometric requirements (one or two dimensions).

The HTR control rod fuel assembly imposes severe geometrical requirements. The assembly itself is a hexagonal shaped block consisting of two B_4C control rods housed in cladding of Incoloy 800. See Figure 7-9. In addition, there exists a symmetric hole, commonly referred to as a "reserve-shut-down-hole." These geometrical factors make equivalent one dimensional representation by such DS_N codes as DTF-IV and ANISN subject to question. To appropriately treat the problem, a two dimensional DS_N code such as TWOTRAN-II or TRIPLET must be employed. TWOTRAN solves the two dimensional multigroup transport equation in (x-y), (r,θ) and (r-z) geometrical mesh allowing for vacuum, reflective, periodic, white, or input specified boundary flux conditions. TRIPLET also solves the two dimensional multigroup transport equation except in planar geometries using a regular triangular mesh finite element method. The boundary conditions available in TRIPLET are essentially the same as TWOTRAN. The increased flexibility of a triangular mesh appears to make TRIPLET the ideal choice of a DS_N code for HTR control rod fuel assemblies. However, it should be noted that the complexities in the TRIPLET solution algorithms caused by the triangular mesh lead to execution times that are about twice as long as those for orthogonal mesh problems[7-15] such as TWOTRAN. On this basis, it is felt that TRIPLET is complementary to, and a replacement for, TWOTRAN, and should be used only when an orthogonal mesh could not possibly give an accurate solution. While a study comparing the inaccuracies between an orthogonal mesh representing a circular hole and a tri-

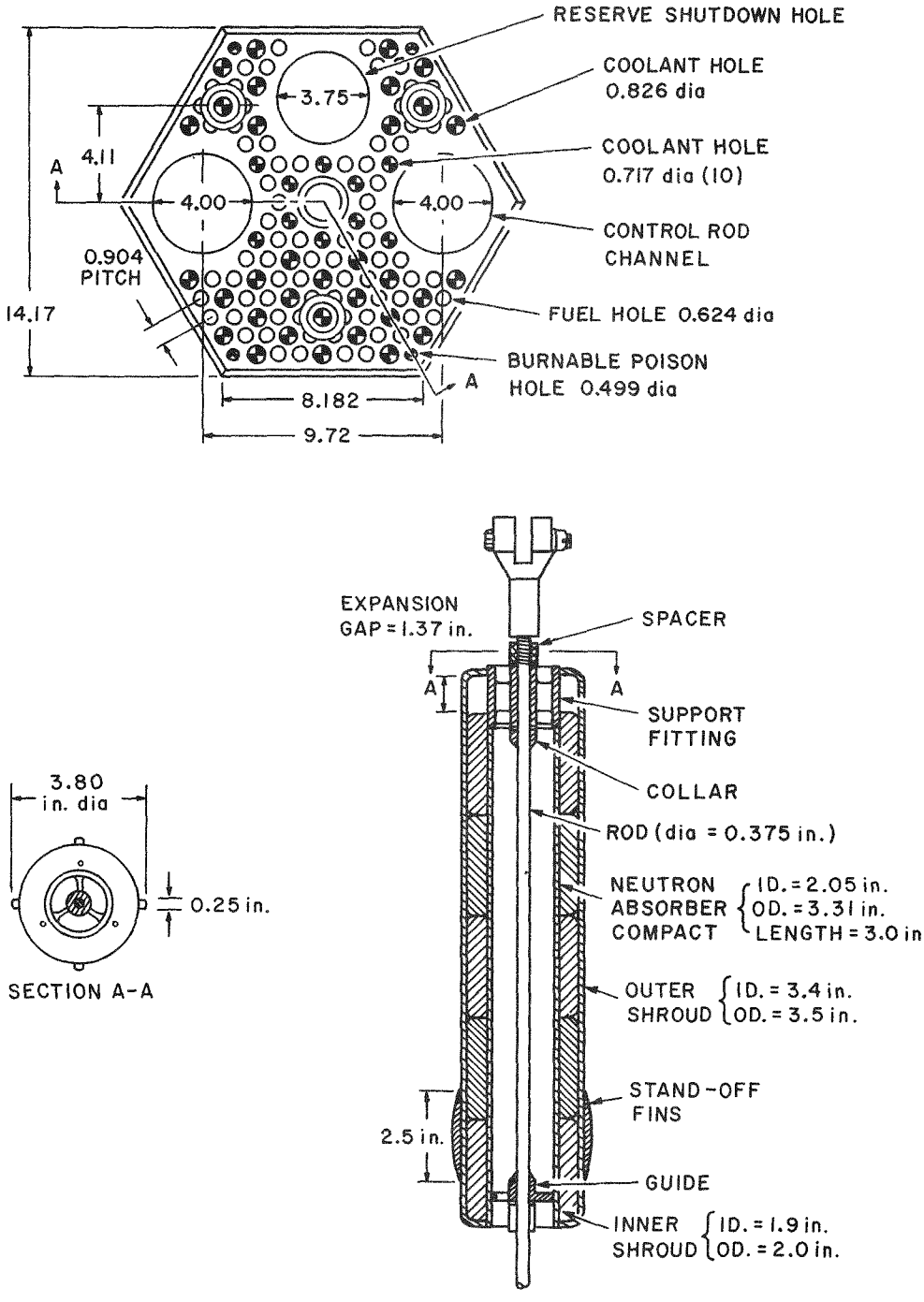

Figure 7-9. Control assembly block and control rod of an HTR (3000 Mw(t)).

angular mesh may be in order, it is believed that at this particular point in time this question need not be addressed.

On the basis of the above discussion, the code TWOTRAN meets the requirements necessary to adequately treat and calculate "group constants" for the HTR control rod fuel assembly. The following sections discuss some of the more important details associated with an accurate representation of the true control rod assembly, the modification necessary to TWOTRAN to group collapse cross-sections over a specific edit zone to generate two group diffusion parameters, and the results of this study.

7.7.2 Geometry and Spacial Mesh Requirements

The geometry of the HTR control rod fuel assembly, discussed in the previous section, lends itself to a reasonable representation in rectangular geometry. TWOTRAN accepts such a geometry with fixed coarse mesh at designated intervals and permits a variable fine mesh within a single coarse mesh. Figure 7-10 describes the TWOTRAN coarse and fine mesh along with the material and material edit zones, used at BNL. The basis for the mesh spacing, material zoning and boundary conditions are discussed subsequently in this section.

Mesh spacing studies for the HTR control rod and its associated assembly have been conducted using the ANISN code. The geometrical layout which forms the basis for this study is shown in Figure 7-11. In these studies several parameters were varied to quantify an appropriate mesh spacing and geometrical layout for TWOTRAN

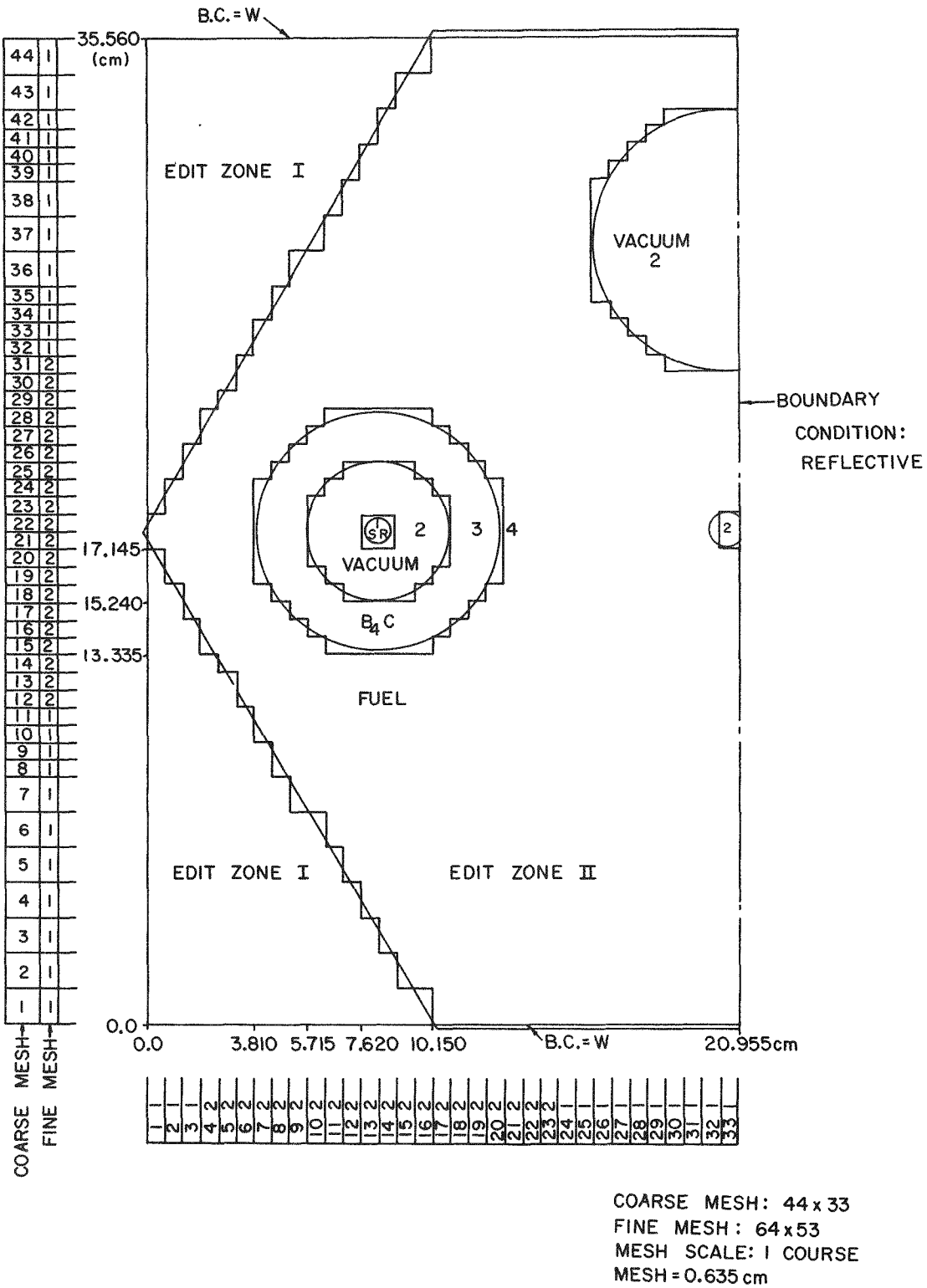

Figure 7-10. TWOTRAN layout of the HTR control rod assembly with control rod.

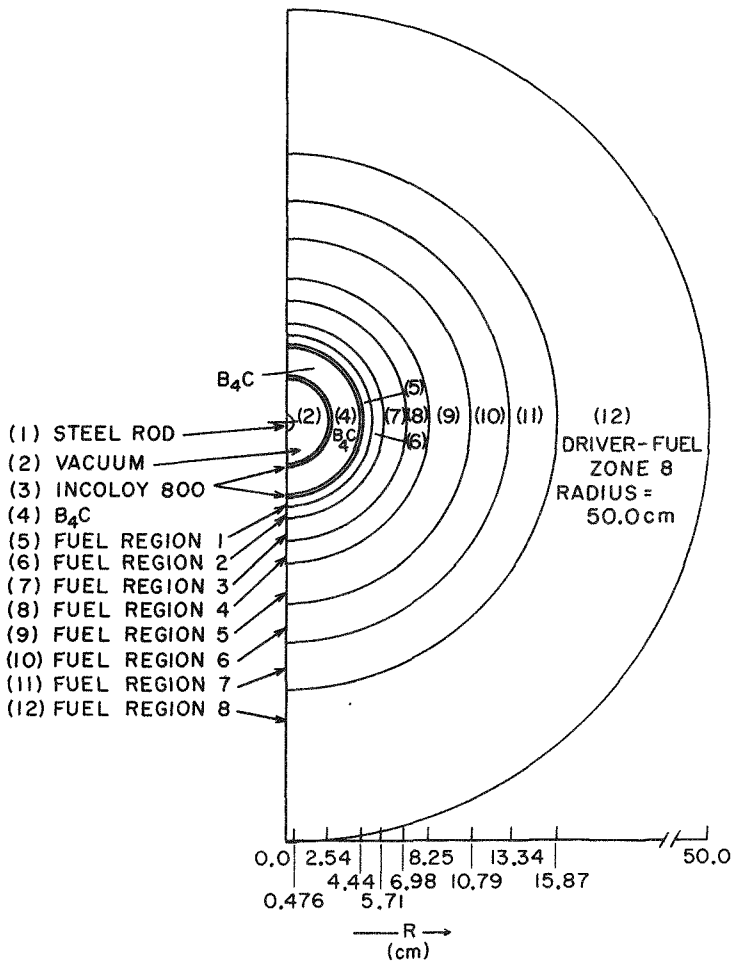

Figure 7-11. Geometric layout of the HTR control rod for ANISN mesh spacing studies.

calculations.

The first study concentrated on the B_4C region of the control rod. Here the mesh was varied from 1 mm per mesh point to 4 mm per mesh point, while holding the mesh spacing constant at approximately 1 mm in all other regions. The main purpose here was to study the numerical effect on the cross-sections of the B_4C, with mesh spacing variation and generate a qualitative feeling for the fast and thermal flux variation through the control rod itself. Figure 7-12 shows a family of thermal flux curves (E = 0.085 eV) as a function of mesh spacing as varied in the B_4C region. While these curves indicate several orders of magnitude variation on the inside edge of the B_4C, it has been found that the overall variation in the "8-group" group collapsed cross sections varied by less than 0.3% in the epithermal range and 0.1% in the thermal range. In addition, a further check on the calculated Eigenvalue indicated a variation of less than 0.2% over all calculations.

A similar study was conducted on the various fuel regions surrounding the control rod with the exception that the upper limit of the mesh spacing was increased to 10 mm per mesh point. The justification here is based on the fact that the flux gradients in the homogenized fuel regions are not as significant as in the B_4C region. As before, the mesh spacing was held constant in all other regions except the fuel. The collapsed cross-section data generated for each of these fuel regions showed a variation of

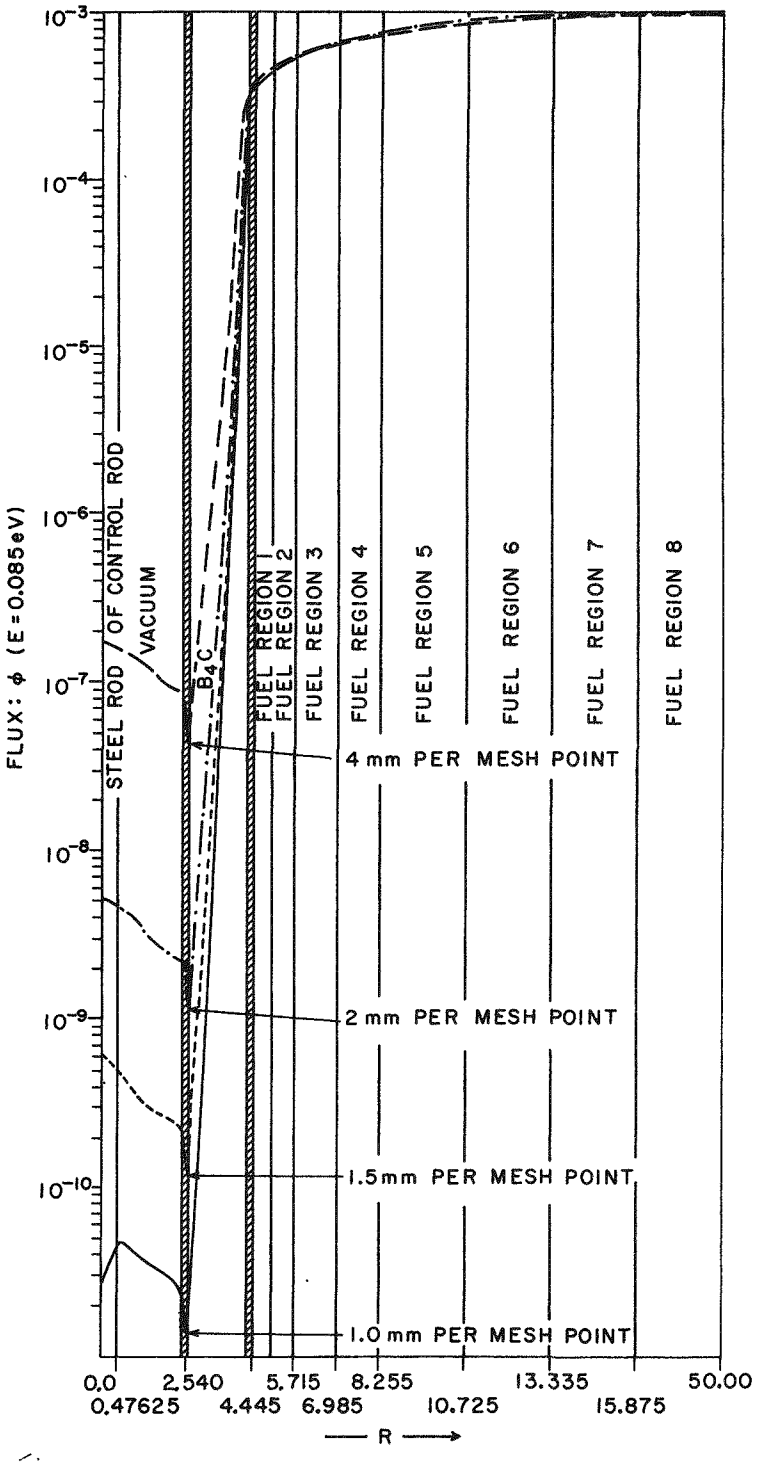

Figure 7-12. Comparison of thermal flux variation within an HTR control rod as a function of mesh spacing using ANISN.

less than 0.1% over all groups when the mesh spacing was varied between 1 and 10 mm. Variation in the Eigenvalue for the system varied by less than 0.08%.

Fuel zoning, which consists of explicitly separate fuel zones, was also studied to determine the spacial dependency of the homogenized fuel cross-sections. All studies indicated a variation of less than 0.01% in cross-sections in fuel regions 1 through 8. See Figures 7-11 and 7-12.

The results of the three above studies indicate the following conclusions:

(1) Acceptable upper limits of mesh spacing by material are:

Region	Mesh Spacing
B_4C	$\leq$ 3 mm
Fuel	$\leq$ 6 mm

(2) One fuel zone region per control rod is acceptable.

7.7.3 Calculational Model

Representation of the HTR control rod assembly was based on TWOTRAN-II. This code, as discussed above, performes few group DS_N calculations on an orthogonal mesh and has been modified to group collapse cross-sections over specific edit regions. Further details regarding the methods employed and other modifications can be obtained from reference 7-16.

The material map for the control rod assembly consists of a 33 x 44 (i-, j-direction) coarse mesh. Figure 7-10 shows the

geometrical layout of the assembly in actual and orthogonal mesh. The coarse mesh intervals were so chosen to conserve volume ratios and remain within the mesh spacing criteria discussed in the previous section. Eight-group cross-sections generated by the GGC-4-ANISN system[7-17] were used. This cross-section set was made up of 4 materials: stainless steel (316), gaseous carbon, B_4C, and mixed moderator fuel ^{235}U-^{232}Th-^{12}C. The B_4C coarse mesh region utilizes the variable fine mesh option in TWOTRAN to provide a tighter computational mesh at and around regions of large flux gradients. Two edit zones were employed to homogenize and group collapse over the assembly.

7.7.4 Results

TWOTRAN-II calculations were performed on the HTR control rod assembly utilizing the homogenization, zone edit, and group collapsing options available. A convergence criteria of 10^{-5} and a quadrature order of 4 is believed to give satisfactory results. The table below lists the final homogeneous two group diffusion parameters for HTR control rod assemblies:

D_1	= 1.64065	D_2	= 1.10811
Σ_{a_1}	= 0.0039185	Σ_{a_2}	= 0.0112355
$\Sigma_{1\to2}$	= 0.0015853		
$\nu\Sigma_{f_1}$	= 0.0000945	$\nu\Sigma_{f_2}$	= 0.0022780
$1/V_1$	= 2.30134×10^{-9}	$1/V_2$	= 2.09118×10^{-6}

References

7-1 L. G. Epel, "Improvement to the GOPTWO Code," BNL Memorandum MF-23, October 10, 1975.

7-2 H. Takahashi, "Finite Element Method Code for Steady-State Heat Conduction, Fission Product Migration, and Neutron Diffusion Calculations (Code DIFFTA)," BNL Memorandum MF-24, November 5, 1975.

7-3 R. E. Funderlic, Editor, The Programmer's Handbook, K-1729 February, 1968.

7-4 A. C. Hindmarsh, "GEAR: Ordinary Differential Equation System Solver," UCID-30001, Rev. 3, December 1974.

7-5 IBM Application Program, System/360 Scientific Sub-routine Package, Version III.

7-6 M. B. Peroomian, A. W. Barsell, and J. C. Saegar, "OXIDE-3 - A Computer Code for Analysis of HTGR Steam or Air Ingress Accidents," GA-A12493 (GA-LTR-7), January 1974.

7-7 HTGR Safety Evaluation Division Quarterly Progress Report, April-June 1975, BNL-50460.

7-8 HTGR Safety Evaluation Division Quarterly Progress Report, July-September 1975, BNL-50479.

7-9 R. D. Richtmeyer and K. W. Morton, Difference Methods for Initial-Value Problems, Interscience Publishers, New York-London-Sydney, 1967.

7-10 P. J. Schneider, Conduction Heat Transfer, Addison-Wesley Book Co., Cambridge, Mass., 1955, pp. 206-12.

References - Cont'd.

7-11 GA-LTR-10 on SORS, General Atomic Co., San Diego, Calif.

7-12 K. D. Lathrop, "DTF-IV, A Fortran Program for Solving the Multi-group Transport Equation with Anisotropic Scattering," Los Alamos Scientific Laboratory Report LA-3373, November 1965.

7-13 W. W. Engle, Jr., "A Users Manual for ANISN, a One Dimensional Discrete Ordinates Transport Code With Anisotropic Scattering," Union Carbide Corporation Report K-1693, March 1967.

7-14 K. D. Lathrop and F. W. Brinkley, "TWOTRAN-II: An Interfaced, Exportable Version of the TWOTRAN Code for Two Dimensional Transport," Los Alamos Scientific Laboratory Report LA-4848-MS July 1973.

7-15 W. M. Reed, "TRIPLET: A Two Dimensional, Multigroup, Triangular Mesh, Planar Geometry, Explicit Transport Code," Los Alamos Scientific Laboratory Report LA-5428-MS.

7-16 A. L. Aronson, BNL Memo to M. M. Levine, "TWOTRAN-II," October 30, 1975.

7-17 J. W. Herczeg, "Group Collapsing of Cross Sections for HTGR's," BNL Memorandum MF-20, July 30, 1975.